EXPLORATION OF THE CU-MN-AS TERNARY PHASE DIAGRAM AND MN_3B_4 ANTIFERROMAGNETS

BY

JINGWEN YU

THESIS

Submitted in partial fulfillment of the requirements
for the degree of Master of Science in Materials Science and Engineering
in the Graduate College of the
University of Illinois at Urbana-Champaign, 2018

Urbana, Illinois

Adviser:

Daniel Shoemaker

ABSTRACT

CuMnAs was first studied more than fifty years ago, both in a tetragonal phase (t-CuMnAs) and orthorhombic phase (o-CuMnAs). Today, the prospect of spintronics has created a new focus on antiferromagnetic materials with Néel temperatures above room temperature, with the goal of reading and writing spin orientations by electrical current. Tetragonal CuMnAs is a candidate whose experimental reading and writing with electrical field has been realized as a proof of concept. Our fundamental knowledge of other phases in the Cu-Mn-As ternary system remains to be improved. In this study, we study a broader part of the phase diagram of this system. We examine the structure of different phases, their thermal and magnetic properties, and the relationship between stoichiometry and structure. We also present our synthetic and magnetic characterization of antiferromagnetic Mn_3B_4. Single crystals larger than 200 microns were obtained and examined by single-crystal diffraction and magnetometry.

ACKNOWLEDGEMENTS

We thank Prof. David Cahill for helpful discussions, Arun Ramanathan for synthesis of Cu-Mn-As samples, Zhelong Jiang for training on laboratory equipment and revisions of this thesis, Dr. Danielle Gray and Dr. Toby Woods in the SCS 3M X-ray diffraction laboratory at the University of Illinois at Urbana-Champaign for their assistance in single crystal X-ray diffraction measurement and structure solution, and the Department of Materials Science and Engineering for financial support. Characterization was carried out in part in the Frederick Seitz Materials Research Laboratory Central Facilities, University of Illinois.

TABLE OF CONTENTS

CHAPTER 1
INTRODUCTION

1.1. Antiferromagnets and CuMnAs

Antiferromagnets have been studied since the 1930s and exhibit the second basic type of magnetic order. [1] Antiferromagnetism is a form of magnetic structure in which the magnetic moments in a material align antiparallel to each other. Although historically this form of magnetism has been difficult to harness for practical applications, recent developments suggest this may soon be about to change. [2]

In the past few years, electrical write/read functionality in experimental memory devices has been verified in semimetallic antiferromagnetic CuMnAs with a Néel temperature of 480 K, deposited by molecular beam epitaxy on silicon and other common semiconductor wafers. [3,9] Sputtered metallic antiferromagnetic films of Mn_2Au with a Néel temperature above 1000 K have also been demonstrated. [4,5]

Candidate materials for antiferromagnetic memory applications need to meet certain selection criteria. To induce spin polarization from spin-orbit coupling, the crystal structure of the material has to satisfy symmetry constraints: either having non-centrosymmetric space group, or centrosymmetric crystals with specific atomic site asymmetries. Detailed structure requirements for spin polarization, as formulated by X. Zhang *et al.* are listed in Fig.1. [7]

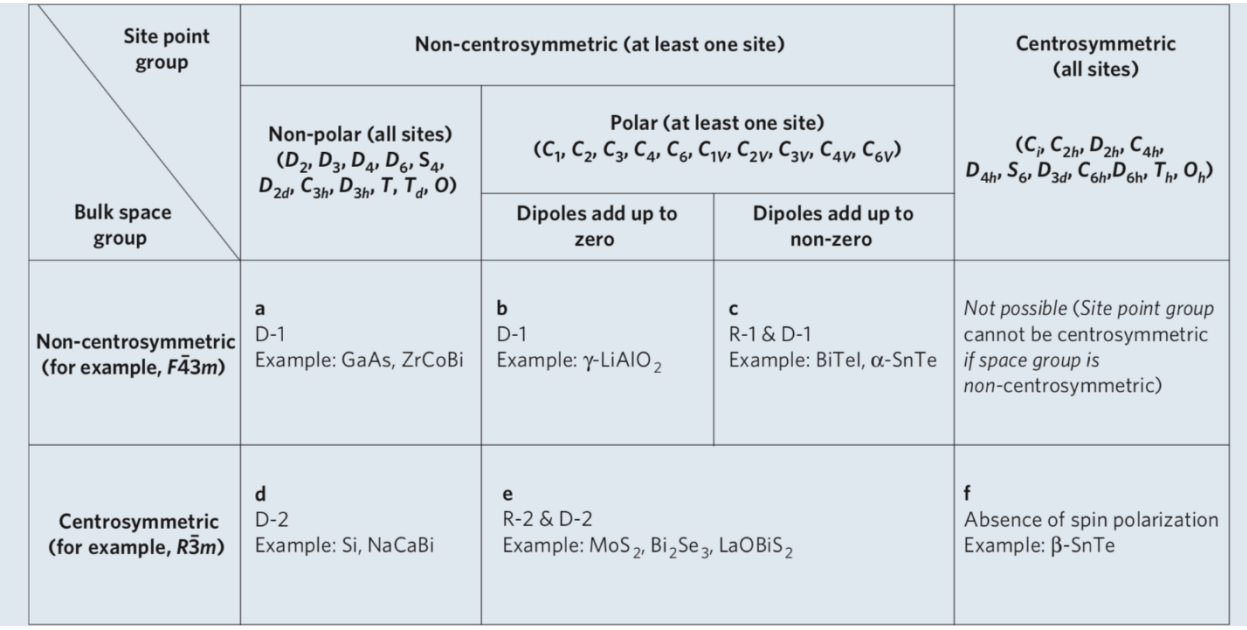

Fig. 1 Classification of spin polarization in nonmagnetic bulk materials on the basis of bulk space group and site point group. Figure reproduced from reference 7.

A representative candidate material for this is CuMnAs. Tetragonal CuMnAs has a centrosymmetric crystal structure with space group *P*4/*nmm* (Fig. 3b). The two Mn spin-sublattices A and B (red and purple) are inversion partners. This results in the crystal having global antiferromagnetism while each sublattice has its own local inversion asymmetry with point group C_s. This crystal structure falls into the D-2 category in Fig. 1. Inverse spin galvanic effects can be generated which lead to nonequilibrium local spin polarizations of opposite signs on Mn atoms of the two sublattices. [8]

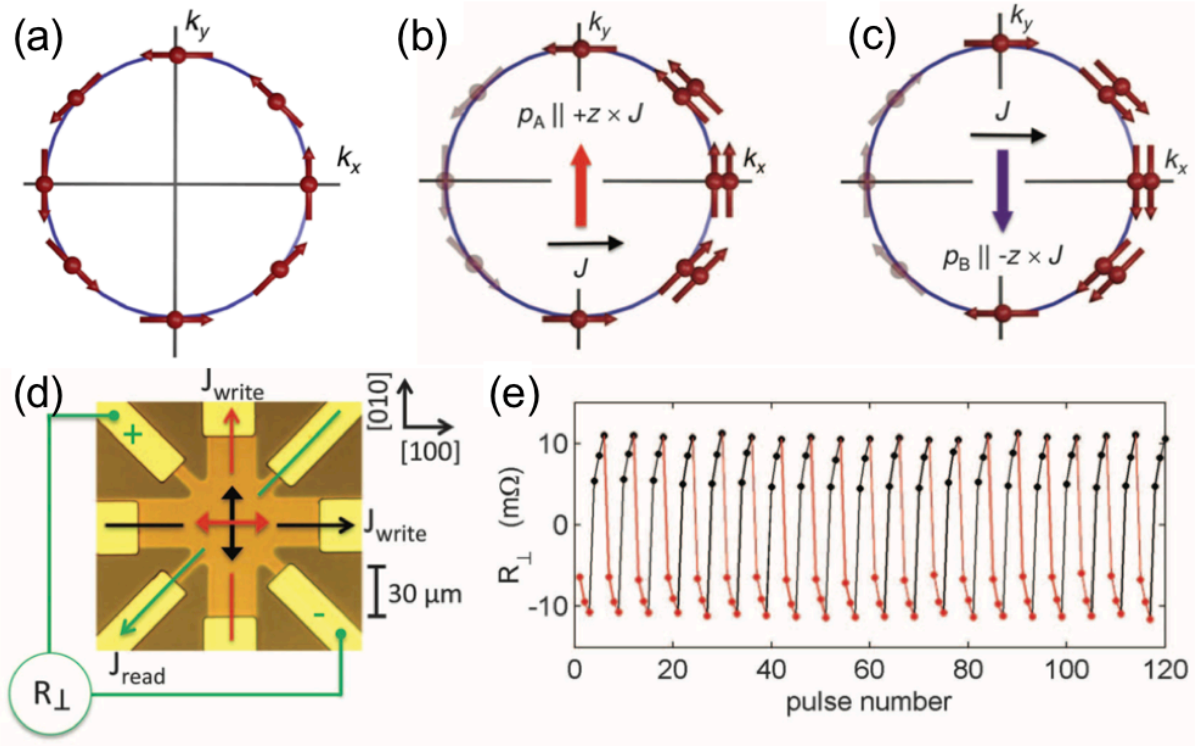

Fig. 2 Rashba spin texture for each sublattice is in equilibrium with zero net spin density (a), and redistributes in electric field (b, c). Schematic (d) of the measurement geometry. Change in the transverse resistance € after applying three successive writing pulses. Figure reproduced from reference 9.

Fig. 2(a) shows that the Rashba spin texture for each sublattice in t-CuMnAs has zero net spin density. The spins redistribute in an applied electric field, resulting in a nonzero spin density due to the local broken inversion symmetry of the spin texture (Fig. 2(b)). Fig. 2(c) is same as (b) for the opposite spin sublattice, resulting in a net in-plane spin polarization in opposite direction. [8,9]

Typical surface patterning for reading and writing measurement geometry is shown by the scheme in Fig. 2(d). After applying three successive 50-ms writing pulses of amplitude J_{write} = 4×10^6A cm^{-2} alternately along the [100] crystal direction of CuMnAs (black arrow in panel D and

black points in panel E) and along the [010] axis (red arrow in panel D and red points in panel E), the reading current J_{read} is applied along the [110] axis, and transverse resistance signals $R_{\perp}$ are recorded 10 s after each writing pulse. A constant offset is subtracted from $R_{\perp}$. Measurements were done at a sample temperature of 273 K. [9]

Reported Cu-Mn-As ternary compounds are CuMnAs (both orthorhombic[23] and tetragonal[24]), $Cu_2Mn_4As_3$, and $CuMn_3As_2$[12]. All of these materials can be considered as pseudobinary compounds of Mn_2As and Cu_2As. Despite the increasing interest, previous research has been mostly concerned about the central part of the Cu-Mn-As ternary system. In my thesis study, we are focusing on building a comprehensive phase diagram by varying the ratio of Cu and Mn while keeping the ratio of As to transition metal as 1:2. The formation of different phases and their magnetic properties are investigated.

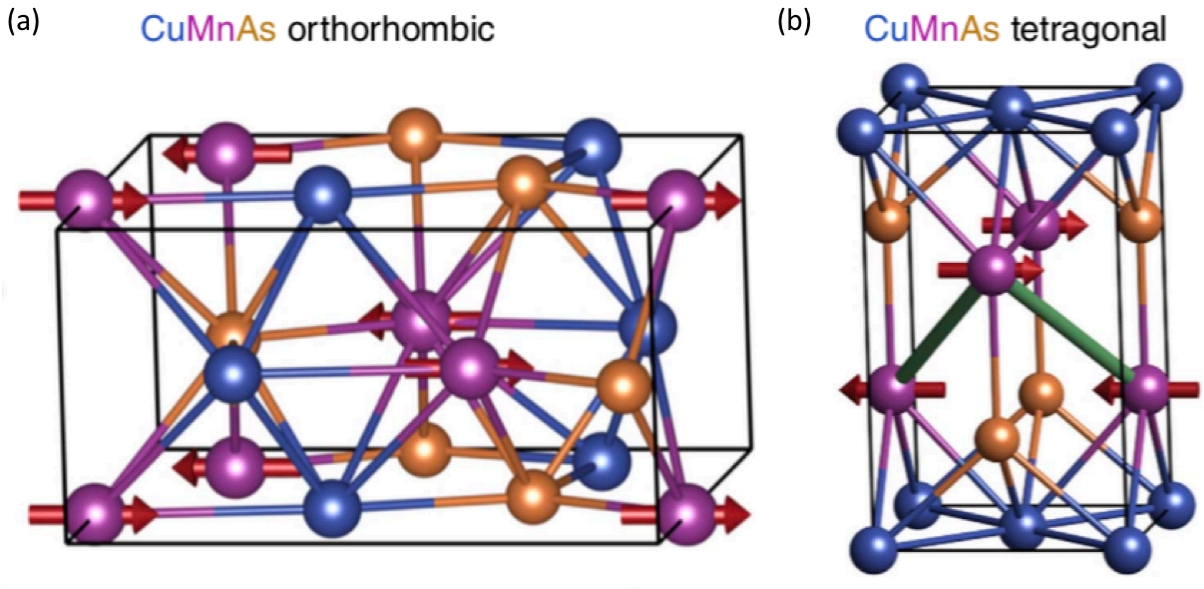

Fig.3 (a). Crystal structure and magnetic structure of orthorhombic CuMnAs. (b). Crystal structure and magnetic structure of tetragonal CuMnAs. (a) and (b) reproduced from reference 11.

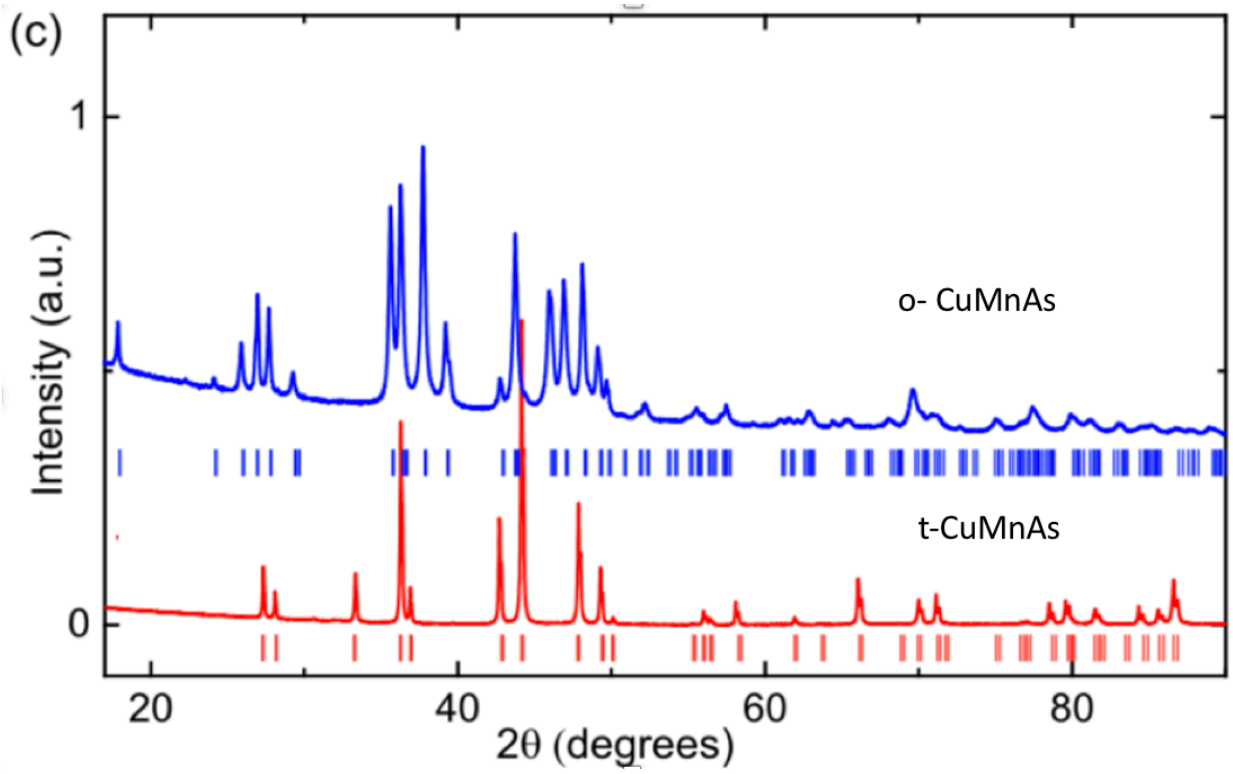

Fig.3(cont.) (c). Powder patterns and major peaks of both phases, reproduced from reference 10.

When synthesized with 1:1:1 Cu:Mn:As stoichiometry, o-CuMnAs is known to form with space group *Pnma* and lattice parameters $a = 0.6577$ nm, $b = 0.384$ nm, $c = 0.73096$ nm (Fig. 3a). It is a 3D network of edge-sharing $CuAs_4$ tetrahedra and $MnAs_5$ square pyramids. [10] The Néel temperature of this orthorhombic phase is 400 K. [14] This crystal structure meets the requirement for D-2 spin polarization in Fig. 1 but has not been investigated in spintronic studies due to its incompatibility with conventional semiconductor substrates. [11]

CuMnAs powders with the orthorhombic phase can be synthesized by solid-state reaction from elements mixed in the stoichiometric 1:1:1 ratio. They were placed into Al_2O_3 crucibles and double sealed inside quartz ampoules. Samples were heated up to 1000°C at a rate of 1°C /min and

annealed for 1 day. [14] Single crystals of mm-scale were reported to be synthesized by flux growth with Bi as the flux. [12,13] The powder XRD pattern of the phase is shown in Fig.3.

The resistivity and magnetic susceptibility of the powder o-CuMnAs was measured by F. Maca, *et al*. Their measurement indicated that 360K is the transition temperature below which the magnetic susceptibility increases with increasing temperature (Fig. 4). This result is consistent with the conclusion that o-CuMnAs is an antiferromagnet with Néel temperature of 360K. [10]

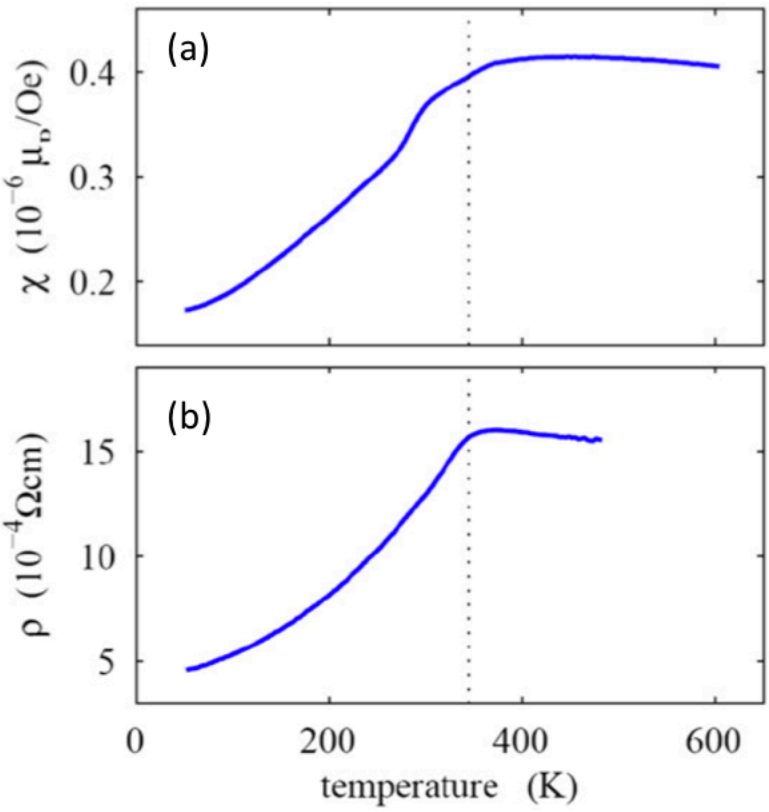

Fig. 4 (a) Magnetic susceptibility of orthorhombic CuMnAs. (b) Temperature dependent resistivity of orthorhombic CuMnAs. Both show clear transition at 360K, indicating the Néel temperature. Figure reproduced from reference 14.

The tetragonal phase of CuMnAs has space group *P*4/*nmm* with Cu_2Sb structure type. The lattice parameters are $a = b = 0.3820$ nm and $c = 0.6318$ nm (Fig. 3(b)). This structure matches

well with the unit cell parameters of GaAs and GaP, which are often-used substrates. The Néel temperature is around 480K. [15]

The synthesis of the tetragonal phase is very similar to that of orthorhombic phase with the practice of solid state reactions. The only difference between producing orthorhombic and tetragonal phases is the precursor stoichiometry. Keeping arsenic to be the same amount (1/3 of the total moles of precursor elements), but slightly raising the Cu/Mn ratio to 1.1, the product will turn out to have tetragonal structure. [16] In spintronic studies, the t-CuMnAs film has been grown on substrates mentioned above by in molecular beam epitaxy (MBE). [11]

Transport phenomena were also measured by P. Wadley *et al.* The resistivity of 140 nm thick CuMnAs showed a room temperature resistivity of around 1.2×10^{-6} Ωm and increases with increasing temperature. It became less temperature dependent above 480 K, which is the Néel temperature of the material (Fig. 5). The Néel temperature was also confirmed by neutron scattering studies. [15]

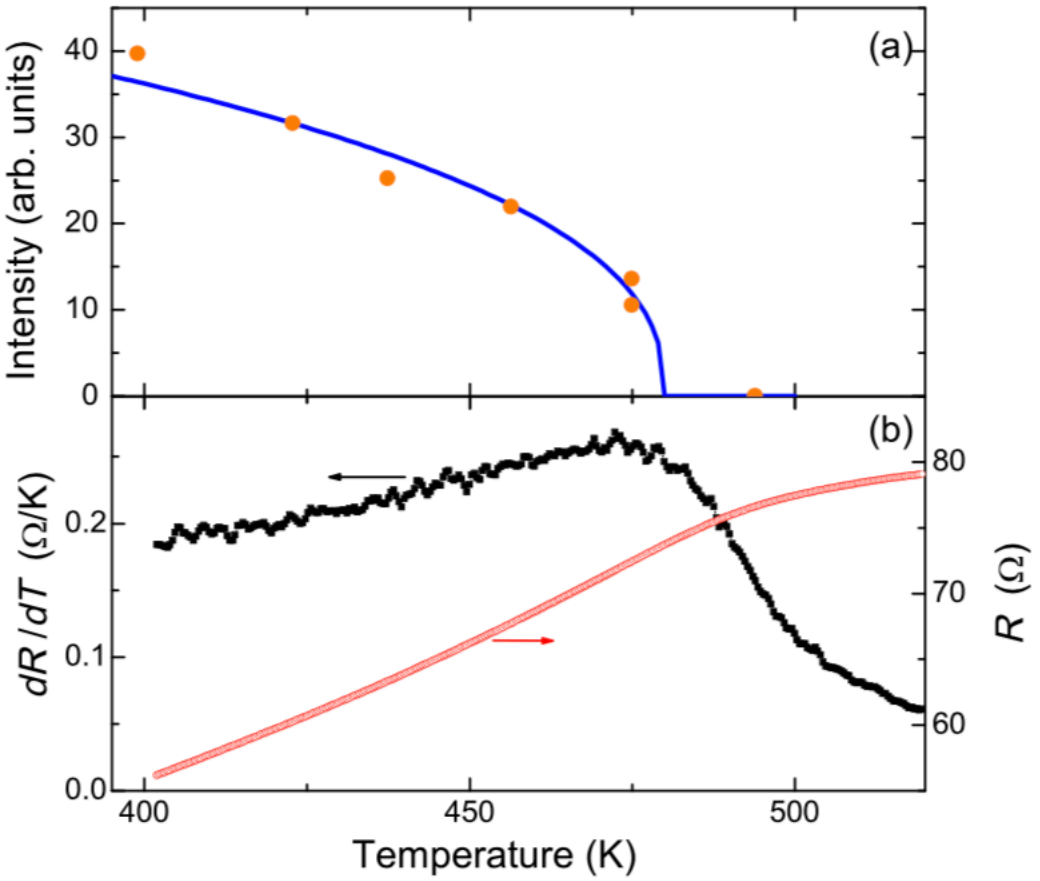

Fig. 5 (a) Intensity of the magnetic (100) neutron diffraction peak versus temperature. The points are the measured data, the line is a fit to power law, yielding a Néel temperature $T_N = 480$ K. (b) Resistivity of tetragonal phase (right axis) and its temperature derivative (left axis) versus temperature which indicate a phase transition at around 480 K. Figure reproduced from reference 15.

Another important member of this family is Mn_2As. Mn_2As also has the Cu_2Sb structure type, with *P*4/*nmm* space group. With similar procedures, the compound is synthesized by solid state reaction of the elements. The Néel temperature for this compound has been reported in the range of 500-600K. [17] Our differential scanning calorimetry work showed that the transition is at around 530 K (Fig. 6(a)).

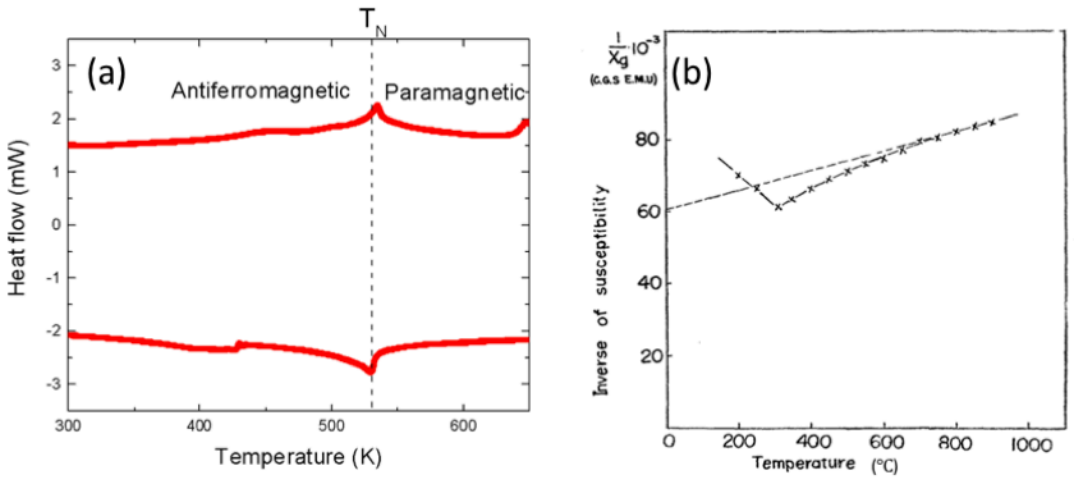

Fig. 6 (a) Our DSC measurements revealed the Néel temperature of Mn_2As around 530K. (b) Magnetic susceptibility measurement done by Motoyoshi, *et al*. in reference 17. The susceptibility data indicate the transition at around 300°C.

The temperature dependent magnetic susceptibility of Mn_2As was measured by M. Yuzuri (Fig. 6(b)). [17] The transition temperature determined from their susceptibility measurement is slightly different than we obtained from DSC, but the difference is within experimental error range.

Mn_2As, t-CuMnAs, o-CuMnAs are three compounds that are relatively well studied in the Cu-Mn-As ternary system. We worked on completing the phase diagram of M_2As (M=Cu,Mn), investigating the Néel temperatures and susceptibilities of different phases. We also report an unknown hexagonal CuMnAs phase with its crystal structure and other properties.

1.2. Symmetry of CuMnAs and some other candidates

t-CuMnAs has space group *P*4/*nmm*. It is a centrosymmetric space group.

Cu atoms occupy the positions with coordinates (-1/4,1/4,1/2), and (1/4,-1/4,1/2). The first two positions are the *2b* Wyckoff positions, with the multiplicity of 2. This site has the symmetry of point group C_{2h}, which is centrosymmetric.

Mn atoms occupy the positions with coordinates (1/4,1/4,*z*), and (-1/4,-1/4,-*z*) (where *z*= -0.1637). These positions are the *2c* Wyckoff positions, with the multiplicity of 2. This site has the symmetry of point group C_{4v}, which is non-centrosymmetric.

As atoms occupy the positions with coordinates (1/4,1/4,*z*), and (-1/4,-1/4,-*z*) (where *z*= 0.23596). These positions are the *2c* Wyckoff positions, with the multiplicity of 2. This site has the symmetry of point group C_{4v}, which is non-centrosymmetric.

Considering the site symmetries, Cu sites show no spin polarization and are nonmagnetic, but Mn sites and As sites are locally non-centrosymmetric. We should be able to observe spin polarization at Mn sites, which, according to Fig. 1, meet the requirement to generate SHE and/or ISGE.

o-CuMnAs crystalizes in the space group *Pnma*. It is a centrosymmetric bulk space group. Cu atoms occupy the positions with coordinates (*x*,1/4,*z*), (-*x*+1/2,3/4,*z*+1/2), (-*x*,3/4,-*z*), (*x*+1/2,1/4,-*z*+1/2) (where *x*=0.6223 and *z*=0.0600). These positions are the *4c* Wyckoff positions, with the multiplicity of 4. This site has the symmetry of point group C_s, which is non-centrosymmetric.

Mn atoms occupy the positions with coordinates (x,1/4,z), (-x+1/2,3/4,z+1/2), (-x,3/4,-z), (x+1/2,1/4,-z+1/2) (where x=0.54020, z=.06780). These positions are the *4c* Wyckoff positions, with the multiplicity of 4. This site has the symmetry of point group C_s, which is non-centrosymmetric.

As atoms occupy the positions with coordinates (x,1/4,z), (-x+1/2,3/4,z+1/2), (-x,3/4,-z), (x+1/2,1/4,-z+1/2) (where $x = 0.2459$ and $z = 0.1234$). These positions are the *4c* Wyckoff positions, with the multiplicity of 4. This site has the symmetry of point group C_s, which is centrosymmetric.

Considering the site symmetries, despite a centrosymmetric bulk space group, all sites are locally non-centrosymmetric. We should be able to observe spin polarizations at Mn sites.

There are other candidate materials that we find interesting. They are antiferromagnetic materials with Néel temperatures above room temperature, and they also have the R-2 or D-2 symmetry. Here we introduce Mn_3B_4, CrAs, and Cr_2As.

Mn_3B_4 crystalizes in the space group *Immm*, a centrosymmetric orthorhombic space group.

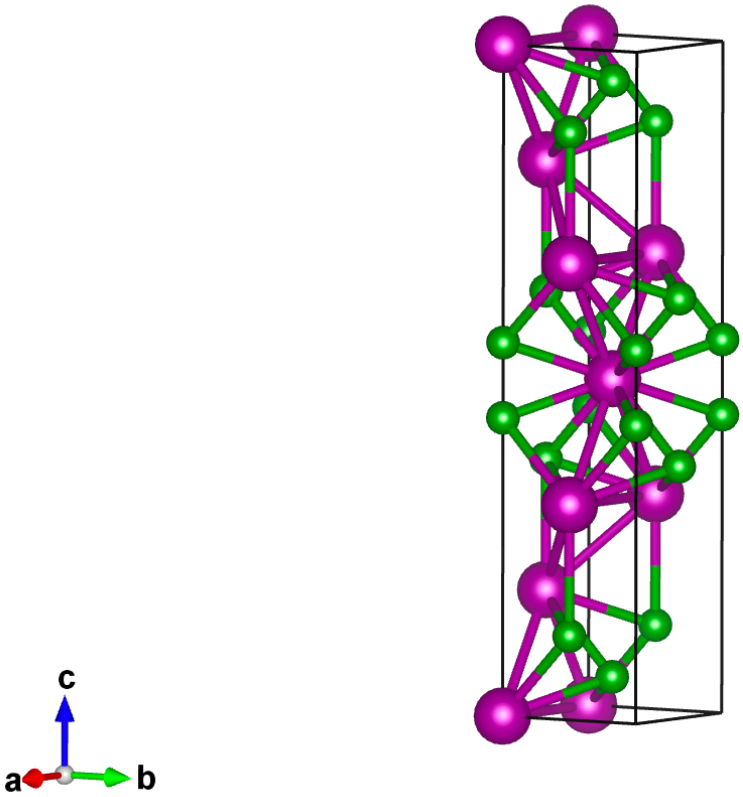

Fig. 7 Unit cell of Mn_3B_4. Purple balls represent Mn atoms, green balls represent B atoms.

In Mn_3B_4, Mn atoms have two different sites, Mn1 sites and Mn2 sites. Atoms on Mn1 site occupy the positions with coordinates (1/2,0,*z*), (1/2,0,-*z*) (where $z = 0.180$). These positions are the *4j* Wyckoff positions, with the multiplicity of 4. This site has the symmetry of point group C_{2v}, which is non-centrosymmetric. Atoms on Mn2 sites occupy the positions with coordinates (0,0,0). This position is the *2a* Wyckoff position, with the multiplicity of 2. This site has the symmetry of point group D_{2h}, which is centrosymmetric.

B atoms also have two different sites, B1 sites and B2 sites. B1 sites occupy the positions with coordinates (1/2,0,*z*), (1/2,0,-*z*) (where $z = 0.375$). These positions are the *4j* Wyckoff

positions, with the multiplicity of 4. This site has the symmetry of point group C_{2v}, which is non-centrosymmetric. B2 sites occupy the positions with coordinates (0,0,z), (0,0,-z) (where $z = 0.444$). These positions are the *4i* Wyckoff positions, with the multiplicity of 4. This site has the symmetry of point group C_{2v}, which is non-centrosymmetric.

Considering the site symmetries, despite a centrosymmetric bulk space group, Mn1 sites are locally non-centrosymmetric. We should be able to observe spin polarizations at Mn sites, which, according to Fig. 1, meet the requirement to generate SHE and/or ISGE.

CrAs crystalizes in space group *Pnma*, a centrosymmetric orthorhombic space group. The phase prototype is MnP.

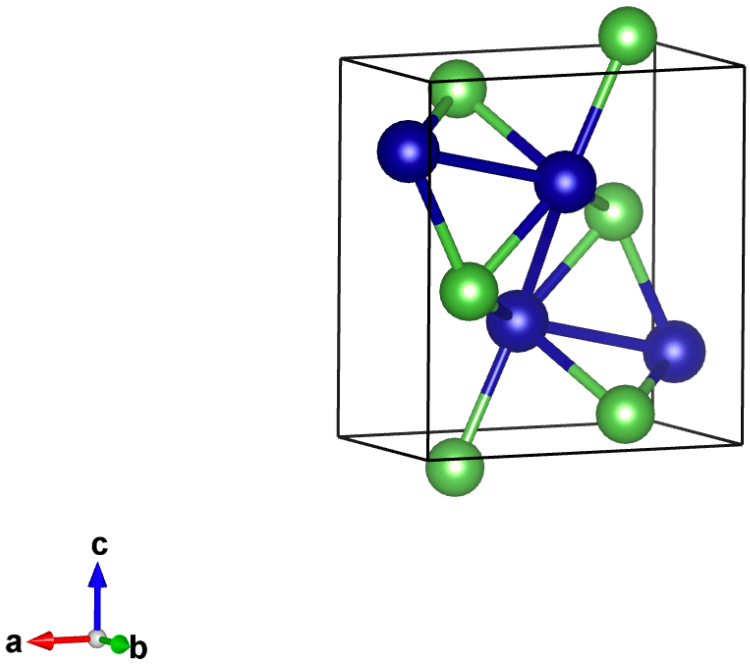

Fig. 8 Unit cell of CrAs. Blue balls represent Cr atoms, green balls represent As atoms.

In CrAs, Cr atoms occupy the positions with coordinates (x,1/4,z), (-x+1/2,3/4,z+1/2), (-x,3/4,-z), (x+1/2,1/4,-z+1/2)) (where x = 0.0033 and z = 0.1993). These positions are the *4c* Wyckoff positions, with the multiplicity of 4. This site has the symmetry of point group C_s, which is non-centrosymmetric.

As atoms occupy the positions with coordinates (x,1/4,z), (-x+1/2,3/4,z+1/2), (-x,3/4,-z), (x+1/2,1/4,-z+1/2)) (where x = 0.1992 and z = 0.5773). These positions are the *4c* Wyckoff positions, with the multiplicity of 4. This site has the symmetry of point group C_s, which is non-centrosymmetric.

Considering the site symmetries, despite a centrosymmetric bulk space group, Cr sites are locally non-centrosymmetric. We should be able to observe spin polarizations at Cr sites.

Cr_2As crystalizes in space group *P4/nmm*, a centrosymmetric tetragonal space group. The phase prototype is Cu_2Sb.

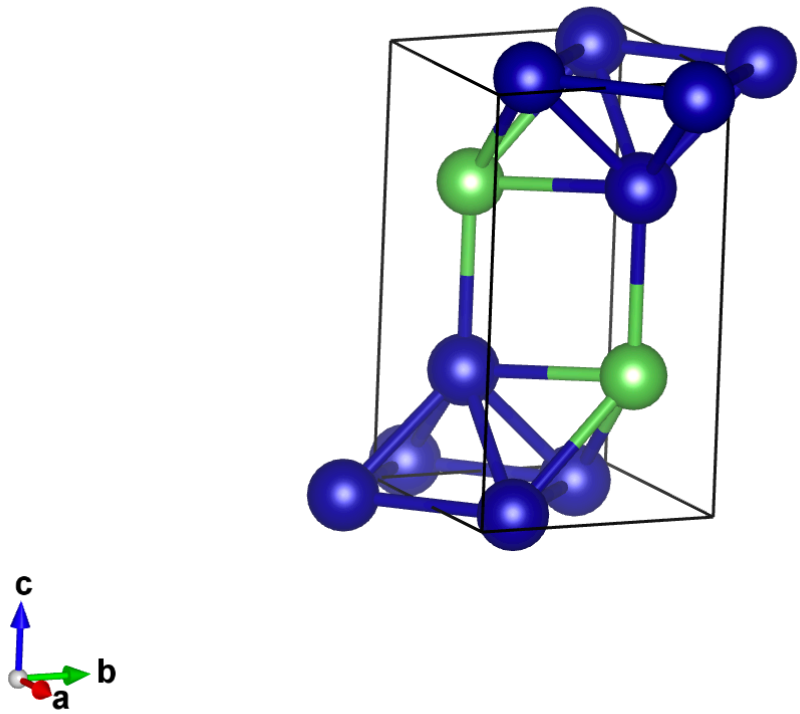

Fig. 9 Unit cell of Cr_2As. Blue balls represent Cr atoms, green balls represent As atoms.

In Cr_2As, Cr atoms have two different sites, Cr1 sites and Cr2 sites. Cr1 sites occupy the positions with coordinates (1/4,1/4,-*z*), (3/4,3/4,*z*) (where $z = 0.675$). These positions are the *2c* Wyckoff positions, with the multiplicity of 2. This site has the symmetry of point group C_{4v}, which is non-centrosymmetric. Cr2 sites occupy the position with coordinates (3/4,1/4,0), (1/4,3/4,0). These positions are the *2a* Wyckoff positions, with the multiplicity of 2. This site has the symmetry of point group D_{2d}, which is also non-centrosymmetric.

As atoms occupy the positions with coordinates (1/4,1/4,*z*), (3/4,3/4,-*z*) (where $z = 0.70$). These positions are the *2c* Wyckoff positions, with the multiplicity of 2. This site has the symmetry of point group C_{4v}, which is non-centrosymmetric.

Considering the site symmetries, despite centrosymmetric bulk space group, both Cr1 and Cr2 sites are locally non-centrosymmetric. We should be able to observe spin polarizations at Cr sites. [27]

CHAPTER 2

METHODS

In our work, X-ray diffraction (XRD) was used to collect the powder diffraction patterns, which help determine the phase of the sample. Single crystal diffraction was used to solve the crystal structures. Differential scanning calorimetry (DSC) was used to characterize the purity and any phase transitions. A Magnetic Property Measurement System (MPMS) was used to characterize the magnetic behavior. These methods are listed in detail below.

2.1. Structural characterization

XRD measurements to determine the lattice parameters were performed on a Rigaku Miniflex 600 equipped with a standard Cu X-ray tube, a graphite monochromator, and a NaI scintillator high speed silicon strip detector. The scanning was done in reflection mode with a 2θ scan range of 3° to 120°. The instrument is operated at the maximum power of 600 W (40kV – 15mA), scanning speed is 2 °/min.

Single crystal X-ray diffraction was conducted on Bruker D8 Venture Duo and Bruker X8ApexII (APEX). DUO is a dual source system equipped with a four-circle kappa-axis diffractometer and motorized Photon 100 CMOS detector capable of shutter-less data collection. Data were collected at 100 K using a Cu source. The Olex2 was used to solve and refine the crystal structure. Crystal structures were visualized using VESTA.

2.2. DSC measurements

DSC was measured on a Q20 from TA Instruments. The experiment cell was loaded with 10 mg sample and the other cell was blank as comparison. Both cells were sealed inside an Ar filled glove box. Both cells were heated up and ramped down between 180 K and 820 K at a ramp rate of 20 K/min. The temperature in both cells was kept the same, and the difference between the heat flows was recorded.

2.3. Scanning electron microscopy (SEM)

Secondary electron images of the solid samples were taken with a JEOL JSM-6060LV microscope with 15 kV acceleration voltage. The SEM samples were placed on carbon tape.

2.4. Magnetic properties measurements

Magnetization measurements on Mn_3B_4 were performed using a Quantum Design MPMS3 operating in DC mode with a sample mass of 14.8 mg in a standard snap-shut powder capsule in a brass trough holder.

CHAPTER 3

RESULTS AND DISSCUSSION

3.1. Cu-Mn-As ternary system

3.1.1. Single crystal structure of hexagonal Cu-Mn-As

All samples were synthesized with powder mixtures of the elements, Cu, Mn, and As in stoichiometric ratios. They were heated to 900°C at a rate of 10°C/min, and held for 12 hours before cooling to room temperature at 1°C/min. The products are either black powders or loose chunks. Powder x-ray diffraction (XRD) patterns were collected on the ground products. Most collected XRD patterns match well with the calculation based on either t- or o-CuMnAs phases from the Inorganic Crystal Structure Database (ICSD). Some impurities of $CuMn_3As_2$ and Cu_5As_3 exist in certain samples as revealed by XRD.

One sample with nominal 59 at% Mn_2As and 41 at% Cu_2As composition had an XRD pattern not matching any known crystal structure. Single crystal X-ray diffraction data was collected to solve its crystal structure.

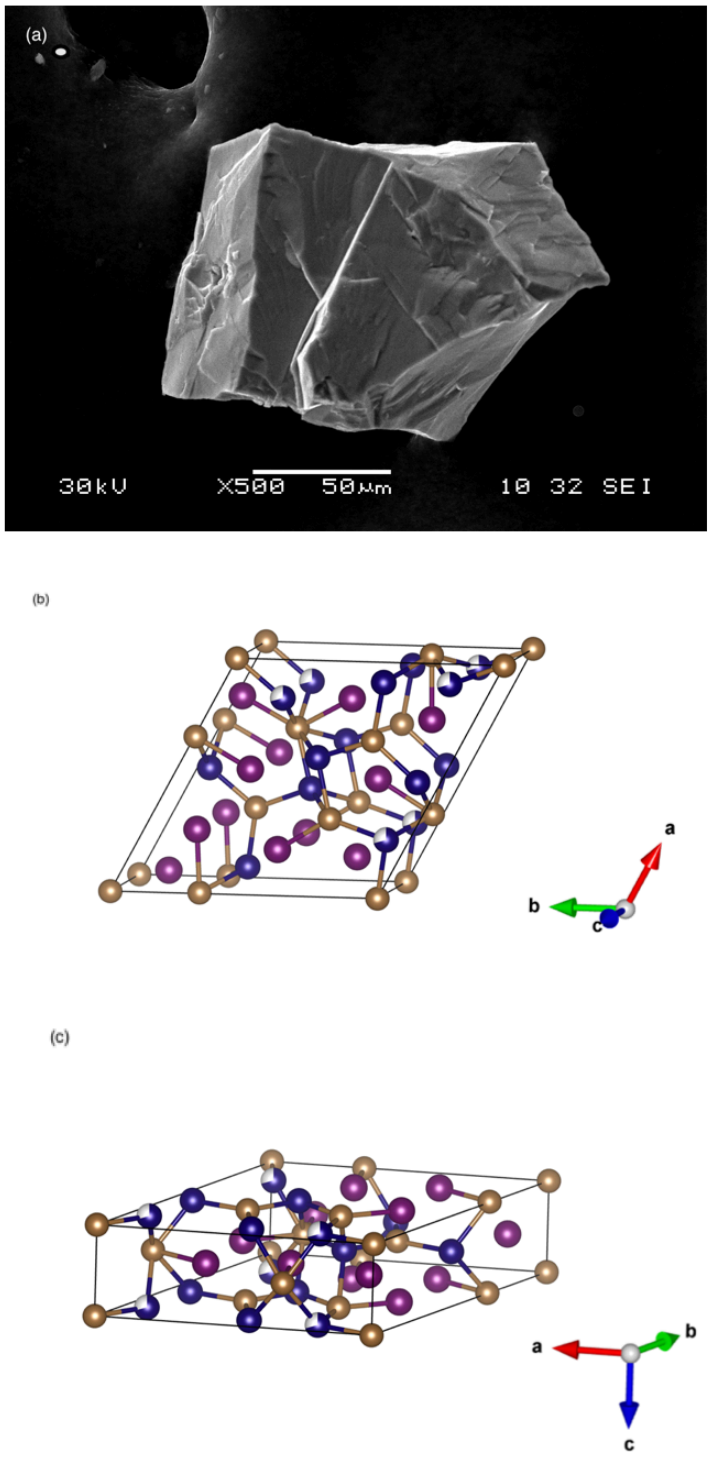

Fig.10 (a) Single crystal SEM image of nominal 59 at% Mn_2As and 41 at% Cu_2As. (b)(c) $P\bar{6}$ Crystal structure solved from the single crystal x-ray diffraction, orientations are noted. Purple spheres indicate Mn atoms, golden spheres are As atoms, and blue/white ones are partially occupied Cu sites.

Scanning electron microscope images were collected for the exact crystal on which single crystal XRD was collected (Fig. 10(a)). It was about 100μm×150μm×50μm in dimension. Its atomic composition was determined to be approximately 34.6 at% Mn, 28.2 at% Cu, 37.2at% As based on energy dispersive X-ray spectroscopy. This crystal is not ideal for single crystal structure determination, as defects such as cracks and twinning can be identified, which add difficulties in solving the crystal structure. Another difficulty arises from the close atomic masses for the constituent Cu, Mn and As elements. Similar electron counts made it more difficult to distinguish between these atoms.

The crystal structure of the above-described crystal after single crystal XRD refinement is listed in the table below. It has hexagonal unit cell with $P\bar{6}$ pace group and lattice parameters of $a = b = 11.14$ Å, $c = 3.83$Å. Cu and Mn atoms each occupy 3 crystallographically distinct atom positions, whereas As atoms occupy 5 positions, including unit cell origin. The Cu2 site has only about 70% occupancy.

Crystal data	
Chemical formula	AsCuMn
M_r	228.85
Crystal system, space group	Hexagonal, $P\bar{6}$
Temperature (K)	296
a, c (Å)	11.1418 (3), 3.8311 (2)
V (Å^3)	411.87 (3)
Z	4
Radiation type	Mo $K\alpha$
μ (mm^{-1})	16.61
Crystal size (mm)	0.12 × 0.08 × 0.04
Data collection	
Diffractometer	Bruker DUO
Absorption correction	–
No. of measured, independent and observed [$I > 2\sigma(I)$] reflections	2124, 950, 912
R_{int}	0.033
$(\sin \theta/\lambda)_{max}$ (Å^{-1})	0.714
Refinement	
$R[F^2 > 2\sigma(F^2)]$, $wR(F^2)$, S	0.029, 0.066, 1.06
No. of reflections	950
No. of parameters	29

Table 1. Crystal lattice parameters determined by single crystal x-ray diffraction method.

	x	y	z	Occ.	site
Cu1	0.42110	0.50310	0.50000	1.000	3k
Cu2	0.24890	0.08580	0.00000	0.669	3j
Cu3	0.58940	0.50410	0.00000	1.000	3j
Mn1	0.19580	0.46730	0.00000	1.000	3j
Mn2	0.80460	0.94180	0.50000	1.000	3k
Mn3	0.80520	0.53110	0.50000	1.000	3k
As1	0.00000	0.00000	0.00000	1.000	1a
As2	0.66667	0.33333	0.00000	1.000	1e
As3	0.33170	0.33610	0.00000	1.000	3j
As4	0.33333	0.66667	0.50000	1.000	1d
As5	0.67560	0.67400	0.50000	1.000	3k

Table2. Coordinates, occupancies and Wyckoff notation for positions of three Cu sites, three Mn Sites, and five As sites in the $P\bar{6}$ structure.

3.1.2. Powder x-ray diffraction: powder pattern does not match the solved structure

Powder x-ray diffraction was also performed on the synthetic products containing the single crystal described previously. The sample powders were packed in a quartz sample holder. The pattern was collected with 3 to 120 degrees 2θ range. The pattern is shown in Fig. 11. The black line is the measured data and the red pattern is calculated from solved structure. The gray line is the difference between two.

All peaks in the powder pattern can be found in the calculated pattern. But there are also calculated peaks that cannot be found in the experimental pattern, including the first three main peaks at low angles (lower than 25 degrees). If the product is composed entirely of the $P\bar{6}$ phase shown in Table 1, the experimental pattern should match completely with calculation (except for statistical noise).

This indicates two possibilities. One is that the crystal structure is not accurate, the other is that the powder sample contains different phase(s). The powder pattern was compared with databases of known materials but no fit was found. This suggests that this powder is not a known material. Since all the peaks in the powder pattern can be found in the calculated pattern, we tend to believe the true structure has the same crystal lattice but with less complexity.

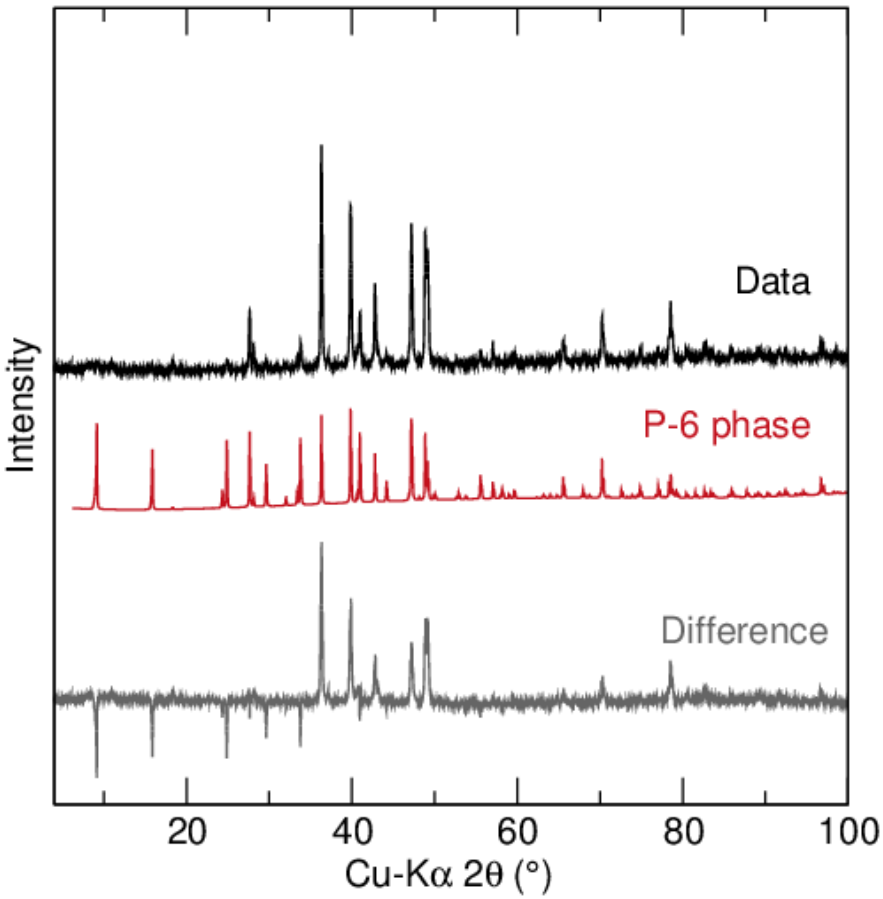

Fig.11 Powder X-ray diffraction pattern on the powder sample (black), calculated pattern from $P\bar{6}$ solved structure (red), and difference between the two (gray).

3.1.3. Differential Scanning Calorimetry (DSC)

DSC is a very sensitive method of detecting temperature induced phase transformations. The samples and reference cells were sealed in Ar-filled glovebox. Differences in heat flow were recorded versus temperature (Fig.12).

During heating, an obvious peak can be seen at around 330K. During cooling, however, the signal suffers from artifacts and the clarity of this transition should be improved.

Considering the feature appeared during both heating and cooling, we tentatively assign it as a reversible transition. The transition could be either structural or magnetic. If this is a magnetic transition, it would be captured by magnetic properties measurement system.

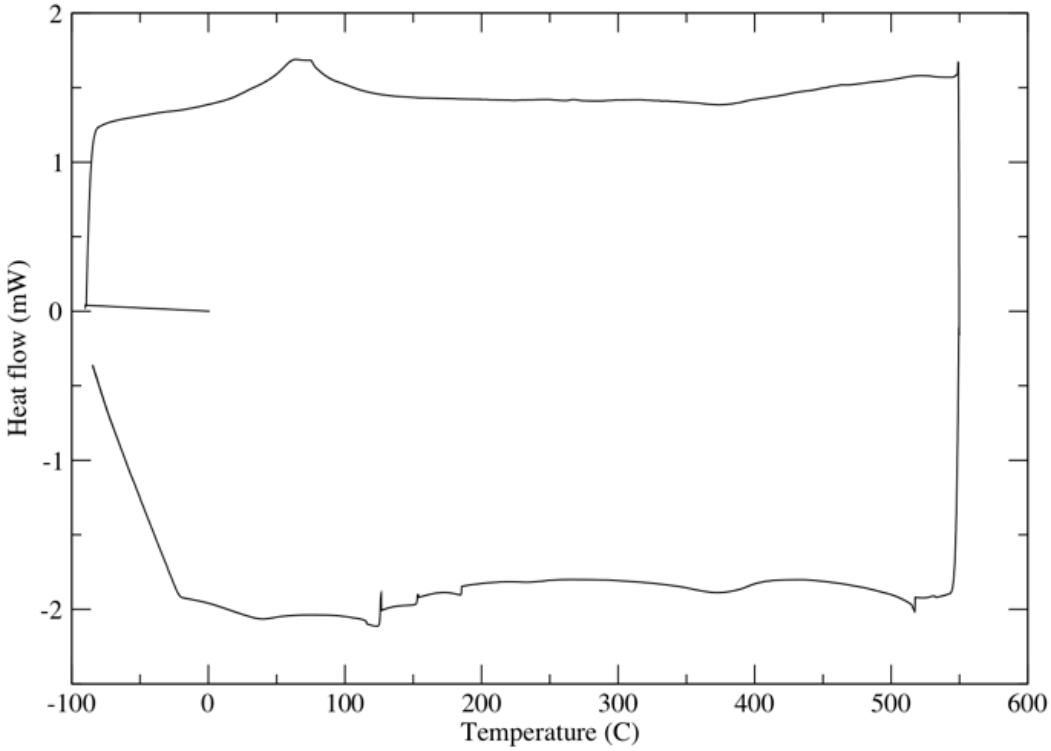

Fig. 12 DSC measurement of the $P\bar{6}$ phase sample. Peaks and bumps may indicate structural or magnetic transitions.

3.1.4. Magnetic Properties Measurement System (MPMS)

The MPMS was used to measure the magnetic susceptibility versus temperature from 5 K to 400 K (Fig. 13).

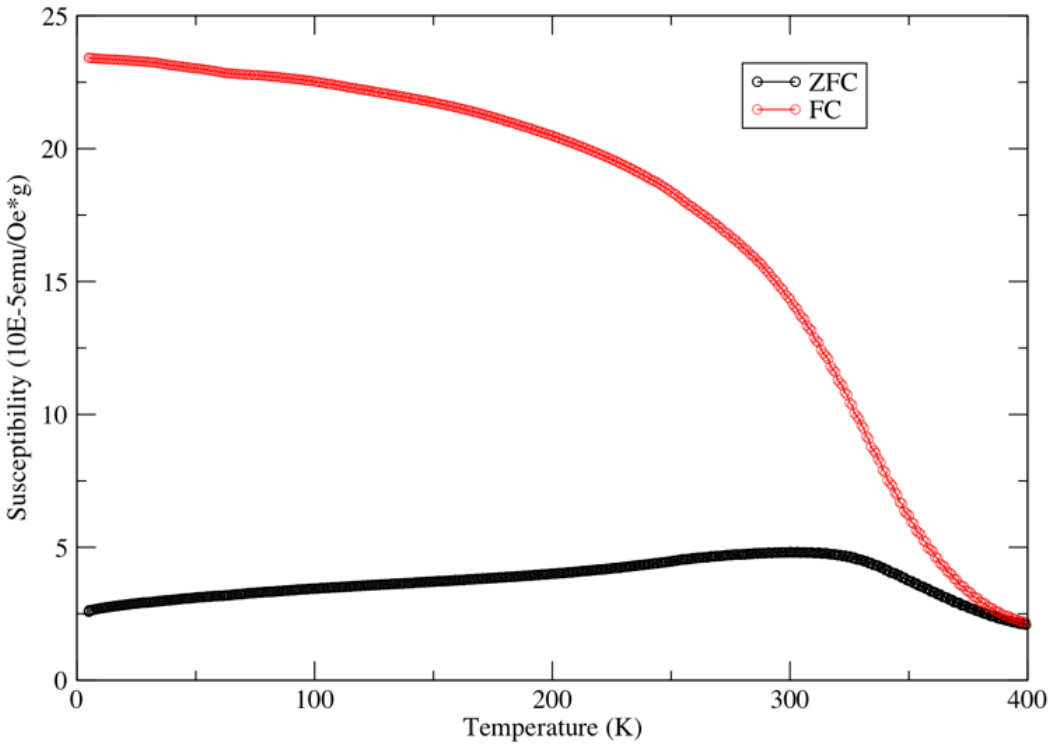

Fig. 13 Susceptibility vs. T curves after zero field cooling (ZFC) and after field cooling (FC) measured at 100 Oe applied fields.

From MPMS, the susceptibility during zero field cooling increased slowly with temperature and reached its peak at around 330 K, which coincides with our tentatively assigned transition temperature from the DSC measurement. The subsequent drop in susceptibility versus temperature is indicative of typical antiferromagnetic behavior.

The irreversibility indicated by the difference between the FC and the ZFC susceptibilities arises from magnetic anisotropy. For a bulk antiferromagnetic material, it is expected to exhibit a peak in the FC and ZFC curves. Due to the temperature range limit, the full view of the shape of

the two curves could not be achieved. Only the ZFC curve has a visible peak. Ideally, the temperature range of MPMS measurement could be extended. Here, we can refer to the reported susceptibilities of other antiferromagnetic materials.

Benitez, *et al*. reported susceptibility data on Cr_2O_3, which has a susceptibility of 3×10^{-4} emu/Oe-g at 40 kOe. [20] This value has the same order of magnitude as our h-CuMnAs susceptibility. Ferromagnetic materials, on the other hand, have far greater susceptibility. $SrRuO_3$ is ferromagnetic and has a susceptibility of 0.09 emu/Oe-g under 100 Oe magnetic field. [21] Based on these values, we believe that h-CuMnAs is an antiferromagnet.

From the DSC and MPMS measurement we can conclude that h-CuMnAs is a new CuMnAs structure that has not been reported before. It has a hexagonal unit cell and behaves like an antiferromagnetic material. The Néel temperature is around 330K. MPMS with extended measurement temperature range should a provide better view of its behavior near the transition temperature, and Curie-Weiss behavior above it.

While investigating this new structure, other compositions in the Cu-Mn-As ternary system were explored. Most of them consist of the tetragonal CuMnAs phase, orthorhombic CuMnAs or $CuMn_3As_2$. These compounds were studied by powder X-ray diffraction and DSC. The Néel temperatures for them are too high (near or above 400K), so MPMS measurement is not useful.

3.1.5. Differential Scanning Calorimetry: Similarities and trends

Based on powder XRD patterns, the phase diagram of Cu_2As-Mn_2As is composed of regions of t-CuMnAs on both the Cu_2As-rich side and the Mn_2As-rich side. Between the two are regions of the orthorhombic and hexagonal phases.

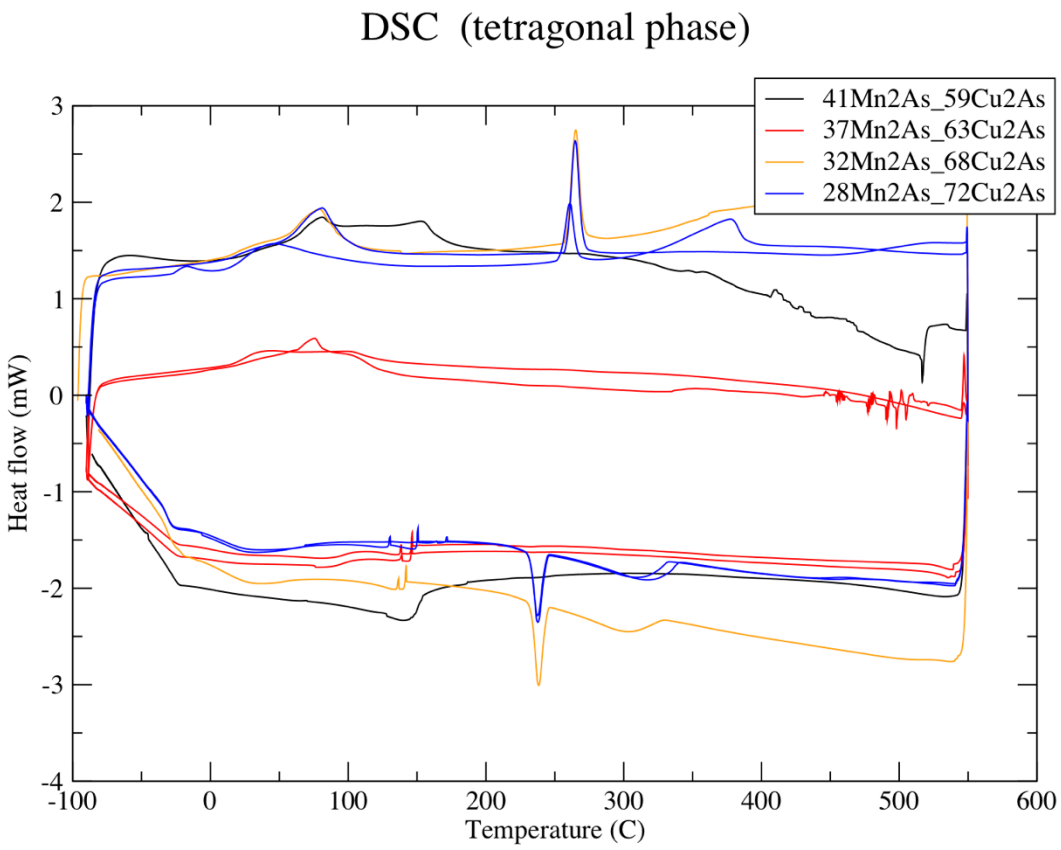

Fig. 14(a) DSC plot of 4 tetragonal CuMnAs compounds of different composition on the Cu_2As rich side of the Cu_2As-Mn_2As pseudobinary.

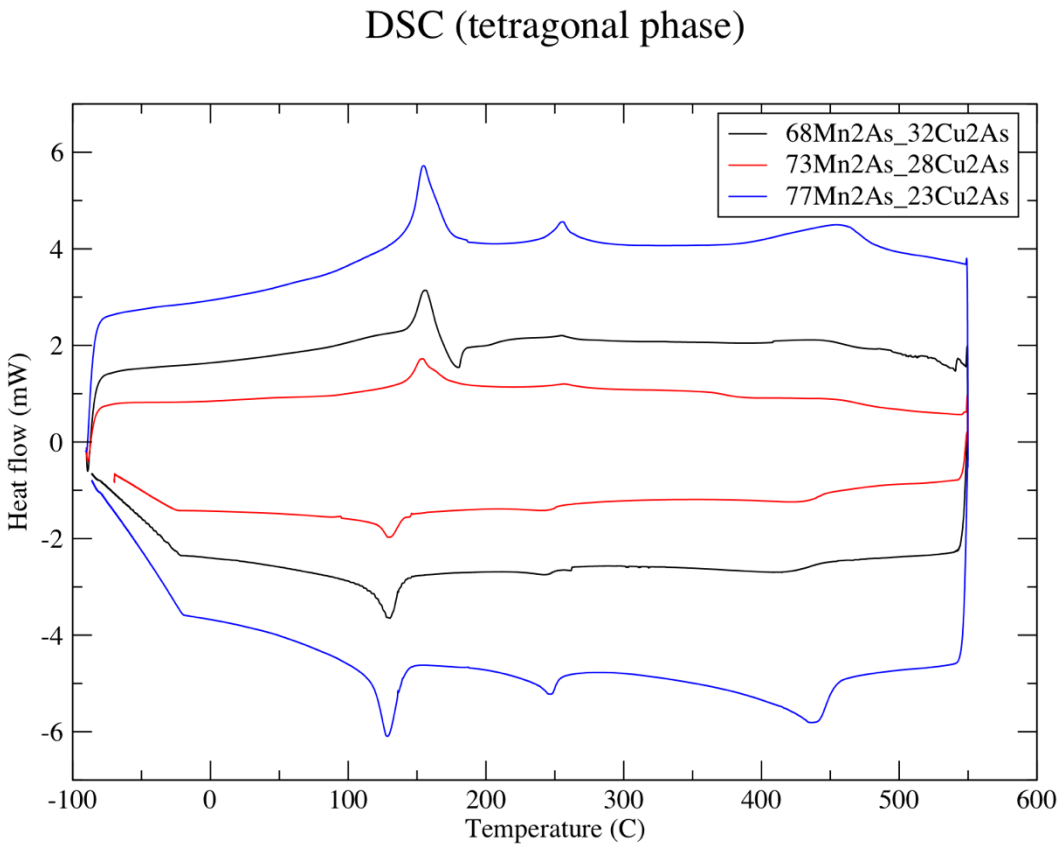

Fig.14(cont.) (b) DSC plot of 3 tetragonal CuMnAs compounds of different compositions on the Mn-rich side of the Cu_2As-Mn_2As pseudobinary.

Fig.14 displays two series of tetragonal CuMnAs compounds in the (a) Cu_2As-rich region and (b) Mn_2As-rich region. From Fig.14(a), as the percentage of Mn_2As increases, the sharp peak near 520 K (250°C) disappears. This peak should correspond to the antiferromagnetic-paramagnetic transition at the Néel temperature. A pair of reversible bumps near 600 K were seen in 28 at%-Mn_2As and 32 at%-Mn_2As samples but not in the others. There are also some features near 370 K that begin to manifest as Mn_2As percentage is increased.

The reported Néel temperatures re 480 K for tetragonal CuMnAs and 360 K for orthorhombic CuMnAs. We observed peaks at 520 K for tetragonal CuMnAs, which we consider to be within the error bars of our DSC measurements. The signal near 400 K is a good match to the orthorhombic phase Néel temperature. As the composition of the compound gets closer to 50 at% Mn_2As – 50 at% Cu_2As, the features in the DSC plots start to resemble those of the orthorhombic phase.

Fig. 14(b) shows the scenario on the Mn_2As-rich side. The peak near 400 K is clearer than that of Cu_2As side. As Mn_2As percentage increases, this peak remains intense while signals near 520 K and 700 K grow stronger. The peak near 520 K could be Néel temperature of tetragonal phase. But the one near 700K is more difficult to assign and could be a structural transition.

To conclude on these similarities and trends, a new plot including all features observed in DSC measurement is provided in Fig. 15.

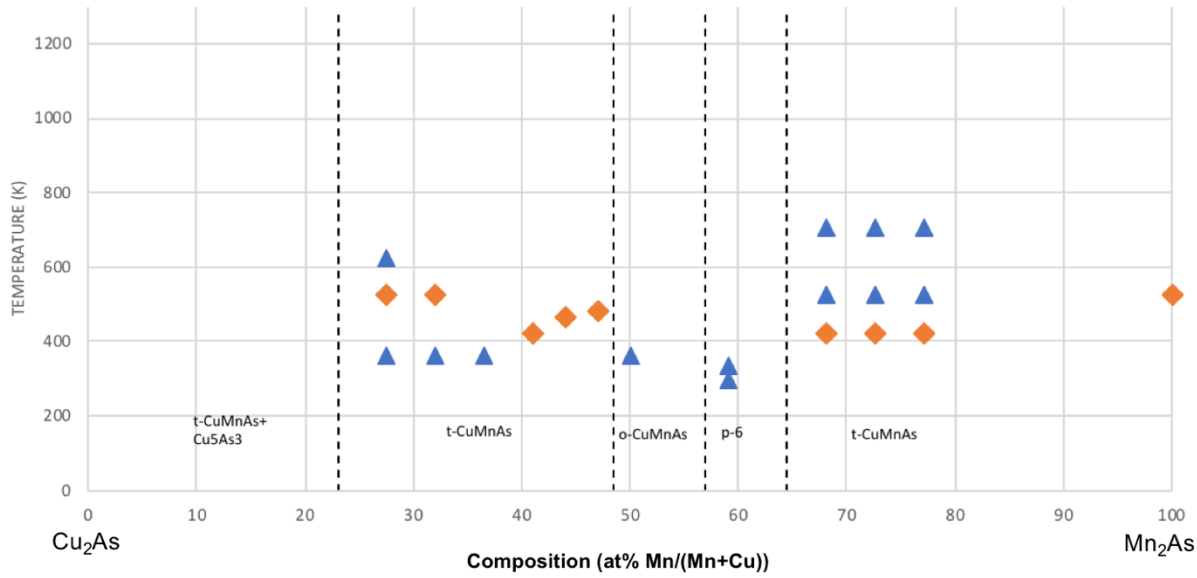

Fig.15 DSC signal chart concluding all the features in DSC measurements. The signals were differentiated by intensities as weak (triangles) or strong (diamonds).

Fig. 15 concludes all the recognizable features from DSC measurements. The signals are represented by triangular and diamond legends based on signal strength. In Fig. 14(a), the most intense peak is near 520 K. As mentioned above, this is believed to be the magnetic transition since it matches with the reported value. In Fig. 14(b), however, the strongest peak is near 400 K, and there are also signals near 520 K. It is likely for the 520 K peak to correspond to the magnetic transition of the tetragonal phase. But since DSC measurements only reveal temperatures of transitions but not the underlying nature, we do not assign the features in Fig.15 to specific transitions due to insufficient supporting evidence to confidently make such assignments. We provide this diagram here to roughly describe features for future studies and reference.

3.2. Mn_3B_4 single crystals

3.2.1. Synthesis

Boron powders (ground from 99.999% purity chunks) and manganese powders (ground from 99.999% purity chunks) in 59:41 atomic ratio were ground, mixed, and sealed in evacuated quartz tubes with 8mm outer diameter. The tubes were sealed to have length shorter than 10 cm. The short length allows the tube to survive longer at high reaction temperatures at which quartz can devitrify or soften. The tubes were heated to 1350°C with a ramping rate of 10°C /min in a GSL-1700X tube furnace (MTI Corporation) and were held at 1350°C for 10 hours. Then the furnace was cooled down at a rate of 5°C/min to room temperature. After reaction, the tubes were coated with a white layer and the product was black soft chunks. The products were broken into small pieces or ground into powders for further characterization.

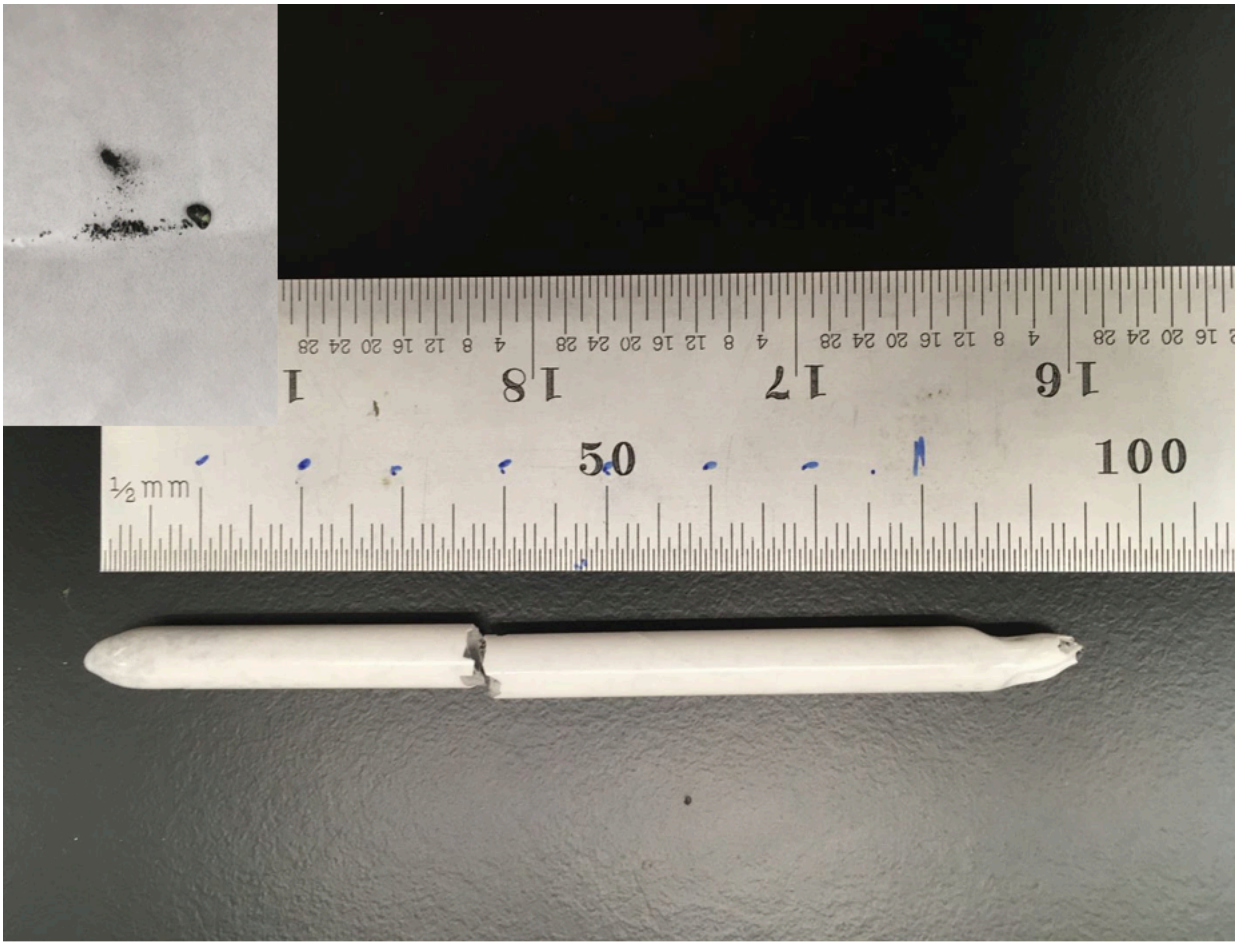

Fig.16 Sealed tube that was used in Mn_3B_4 synthesis, shorter than 10cm, and black chunks and powder product (upper left).

3.2.2. Scanning Electron Microscopy (SEM)

To gain an overview of the sizes of the crystals, products were observed under the SEM. The vast majority of the product consists of small (tens of microns) particles with round edges and rough surfaces. Besides these particles, there were also plates of different shapes. Shown in the left panel of Fig. 17 was one of the largest plates observed, having trapezoid-like geometry with 300-micron length on the longest side. The majority of plates are smaller, however, with diagonal lengths near or below 100 microns.

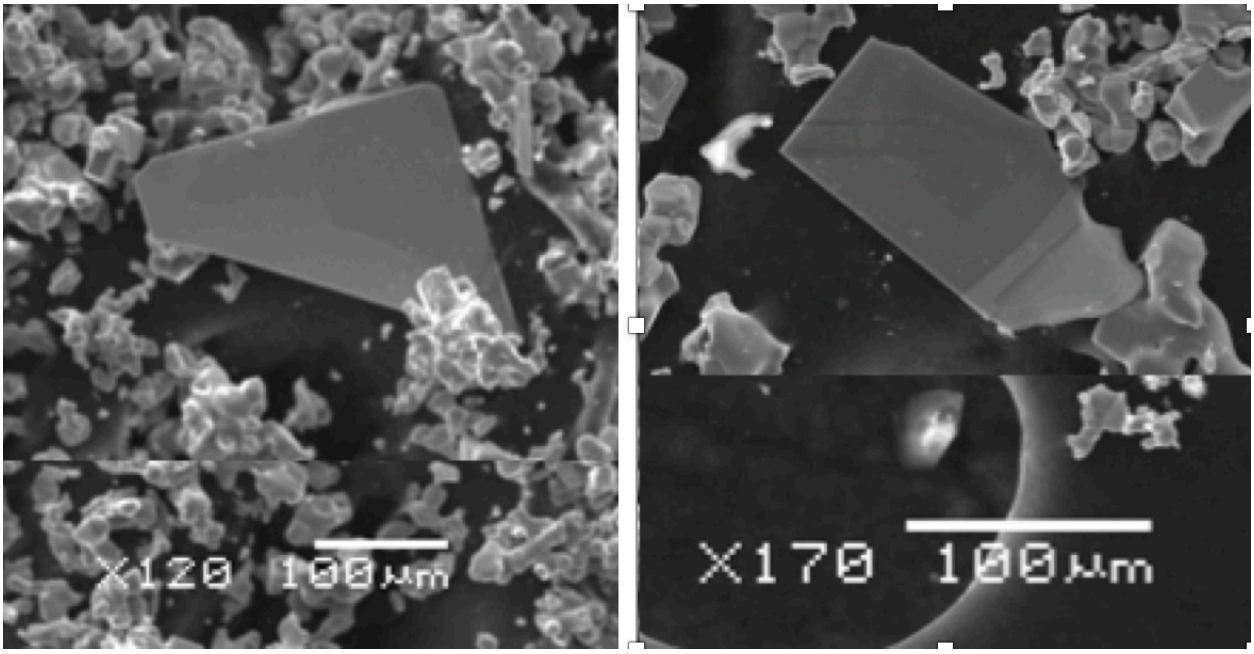

Fig.17 SEM images of different Mn_3B_4 plates observed in the 1350°C 10 hours batch product. The one showed in left image was the biggest one found. The one on right was of average size.

Since some plates exceed 100 microns, they can be identified visually as pieces having shiny facets then the product chunks are broken. Large crystals are required for further characterization, such as quadratic magneto-optic Kerr effect measurements.

In the process of obtaining crystals with larger sizes, we found the crystal sizes to be dependent on synthesis conditions. In particular, reaction temperature has a dominant impact on crystal sizes.

The same procedures for preparing powder mixtures and sealed tubes as described above were used on multiple batches of experiments. The only difference between each batch was the highest holding temperature. All other factors, including ramping rates, tube length, and raw

material amounts were maintained constant. Products of each batch were observed under SEM. Images in Fig. 18 show the biggest crystal that was found.

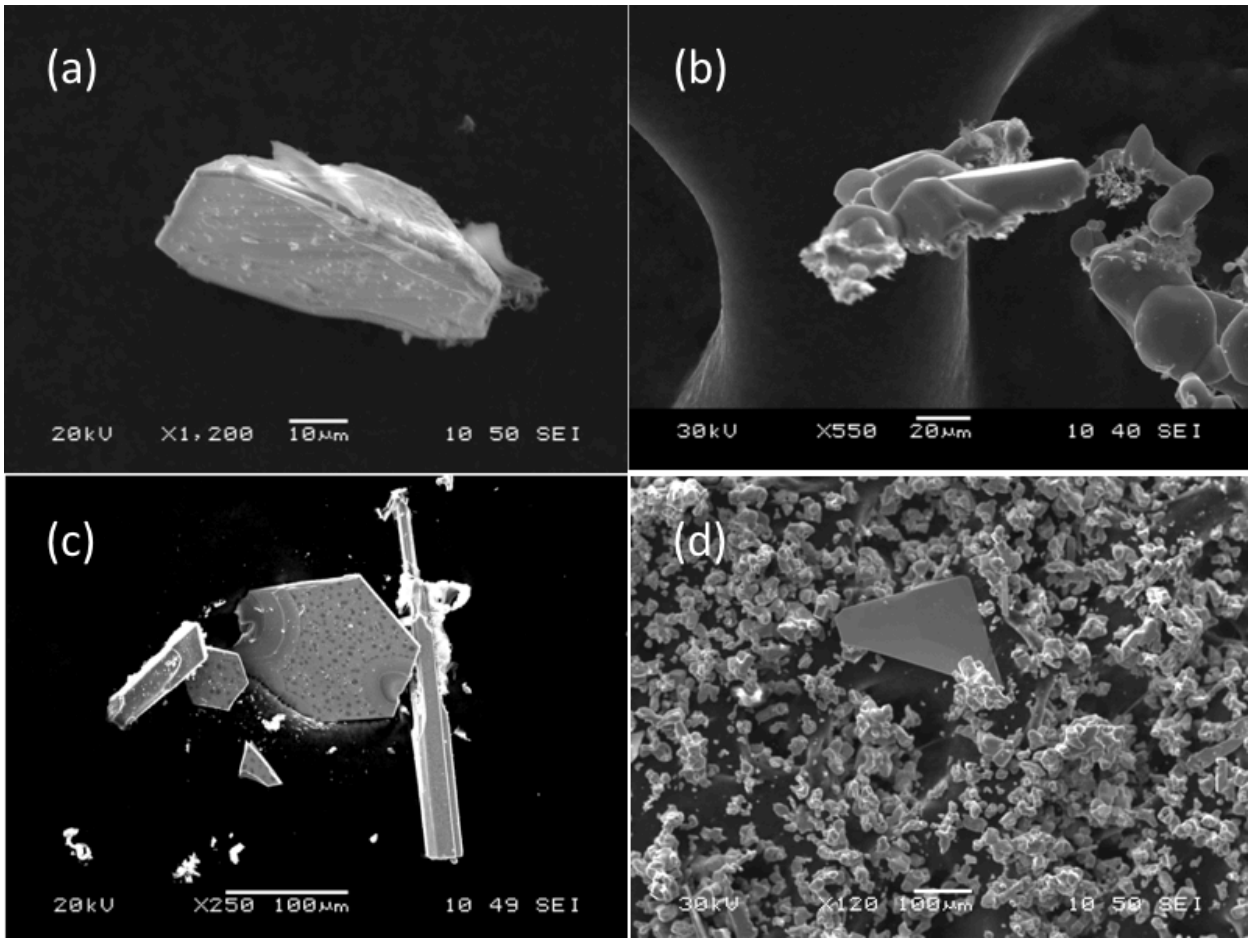

Fig. 18 SEM images taken for crystals synthesized by heating treatment at 1100°C for 48 hours (a), 1100°C for 7 days (b), 1300°C for 10 hours (c), and 1350°C for 10 hours (d).

Crystals in image (a) and (b) are both produced with 1100°C maximum heating temperature, with (a) 48 hours and (b) 7 day holding times, respectively. The crystal in Fig. 18(a) is about 50 microns long and 10 microns thick and has many small particles on the surface. The crystal in Fig. 18(b) has a flat surface about 60 microns long. Simply extending the heating time did not improve crystal size or quality.

Fig. 18(c) was taken from the batch heated up to 1300°C and held for 10 hours. The reactions could not be performed for longer durations due to the softening of quartz at 1300°C. But even with only 10-hour reaction time, the crystals produced were larger. There are hexagonal plates (up to 150 microns across) and a needle (near 300 microns long) in the image. Both types of crystals were picked and analyzed with single crystal x-ray diffraction. It turned out that the hexagonal plates are orthorhombic Mn_3B_4 (*Immm* space group with $a = 0.296$ nm, $b = 0.3032$ nm, and $c = 1.286$ nm) and the needles are MnB impurities (orthorhombic *Pnma*).

Increasing the temperature to 1350°C (with 10-hour holding time) produced further improved crystals (Fig. 18(d)). Plates with length over 300 microns could be isolated. From these batches of experiments, it is concluded that maximum temperature is more important than heating time for large crystal production.

3.2.3. Powder X-ray diffraction

Powder x-ray diffraction was performed on powder products from each batch to ensure phase purity. Fig. 19 shows the powder pattern of the products from same batch as the crystals in Fig. 18(c). The calculated pattern is based on the known structure of Mn_3B_4.

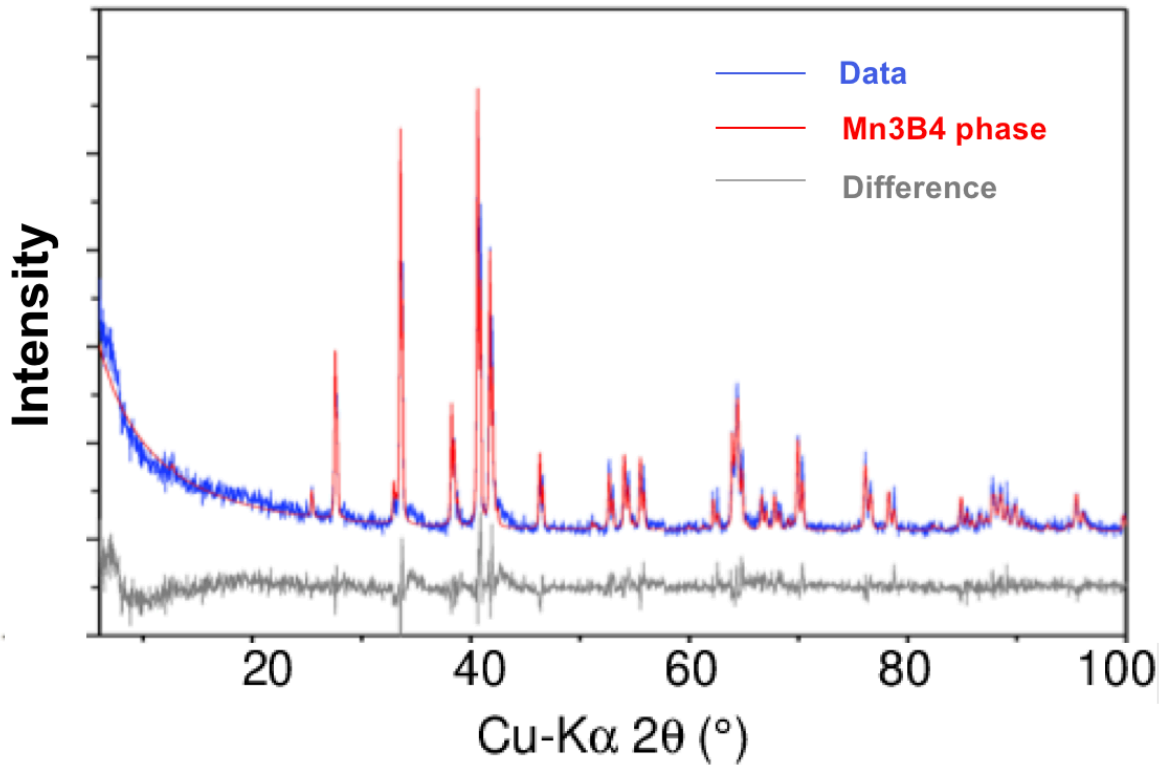

Fig.19 Powder X-ray diffraction pattern on the powder sample (blue), calculated pattern from solved structure (red), and difference between the two (gray).

The MnB phase seen in the Fig. 19(c) was not observed in this powder pattern, even though the SEM image and powder XRD were taken from the same batch sample. The amount of the MnB impurity is likely too small to be seen in powder XRD.

In this case, powder XRD is not a reliable method to test if particular plates are the desired Mn_3B_4 phase. We conducted single crystal x-ray diffraction and collected unit cell data on dozens of plates and needles to find out the relationship between crystal shapes and structural phases. It turned out that all thin plates are orthorhombic Mn_3B_4 and all needles are MnB.

For future characterization focused on Mn_3B_4, it is important to pick plate-shaped crystals and index them via single-crystal diffraction.

3.2.4. Precession images

In single crystal X-ray diffraction, the precession method is an inefficient mode of data collection, as only reflections from a single reciprocal lattice plane are recorded. But precession diagrams can show the reciprocal planes without any distortion. With these images it is much easier to observe the symmetry of reciprocal space. Precession images were taken on both plates and needles (Fig. 20). The left panel were images of plates and right panel were images of needles.

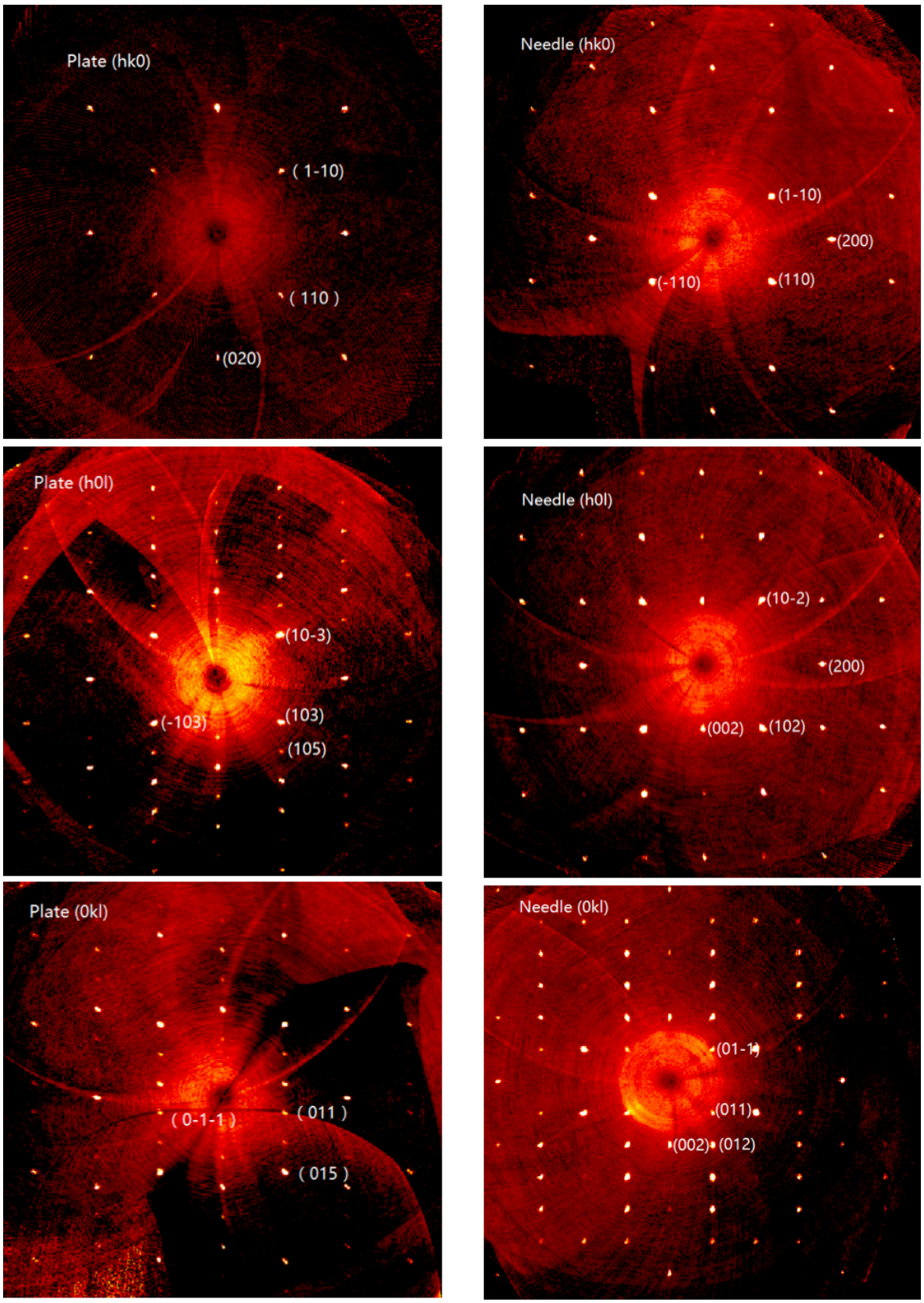

Fig. 20 Precession images for plates (orthorhombic Mn_3B_4) and needles (MnB).

Single crystal diffraction also showed the crystallographic plane for the smooth surface of the plate crystals. The figure below was captured during the determination of crystal size. The largest, flat surface of the plate corresponds to the (001) plane.

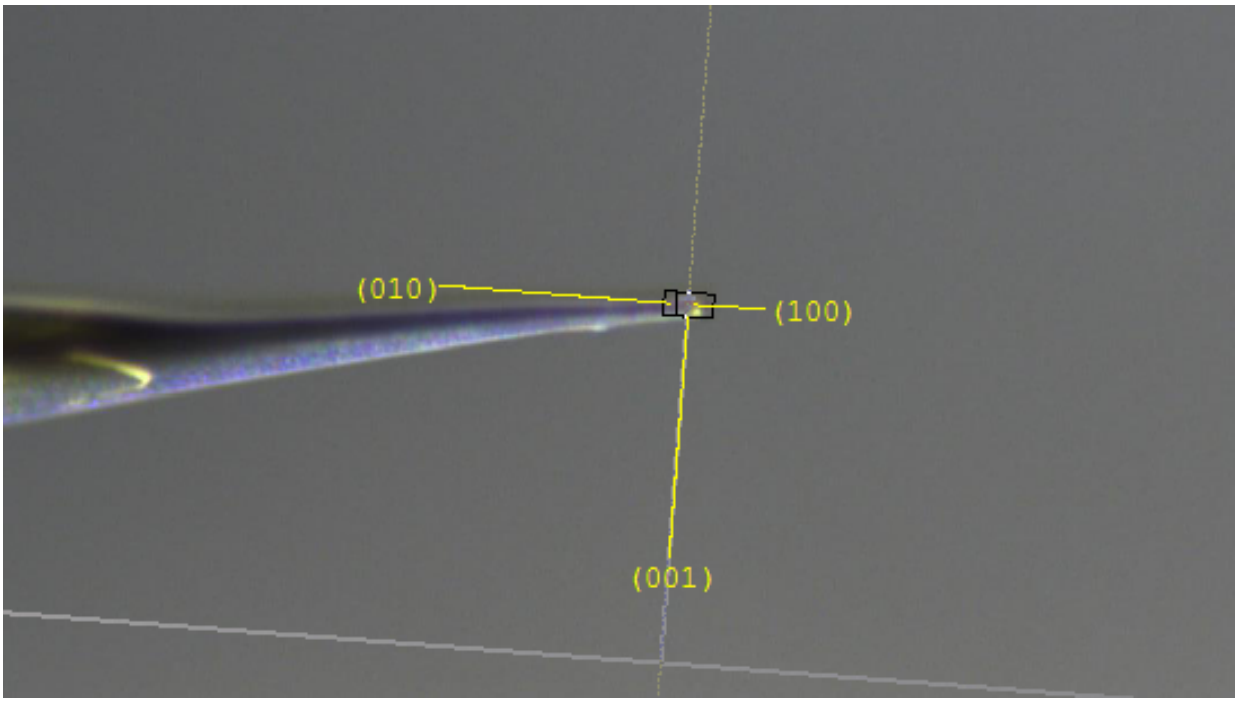

Fig. 21 Picture taken from video while determining crystal size and faces.

3.2.5. Magnetic Properties

Mn_3B_4 is a typical antiferromagnetic material whose magnetic properties were first reported by Hirota and Yanase[25] in 1965. Neutron diffraction studies on Mn_3B_4 were first published by Neov and Legrand[26] in 1972. The Néel temperature was determined to be 392 K, above room temperature, with a subsequent antiferromagnetic ordering at 226 K.

Magnetic susceptibility versus temperature is plotted in Fig. 22. Higher measurement temperature is needed to observe magnetic behavior near and above 400 K. However, splitting between the ZFC and FC curves started to manifest below around 400 K, which agrees with the reported Néel temperature of 392 K. The second downturn at 226 K corresponds to the magnetic ordering of the second Mn sublattice, as described by Neov and Legrand. [26]

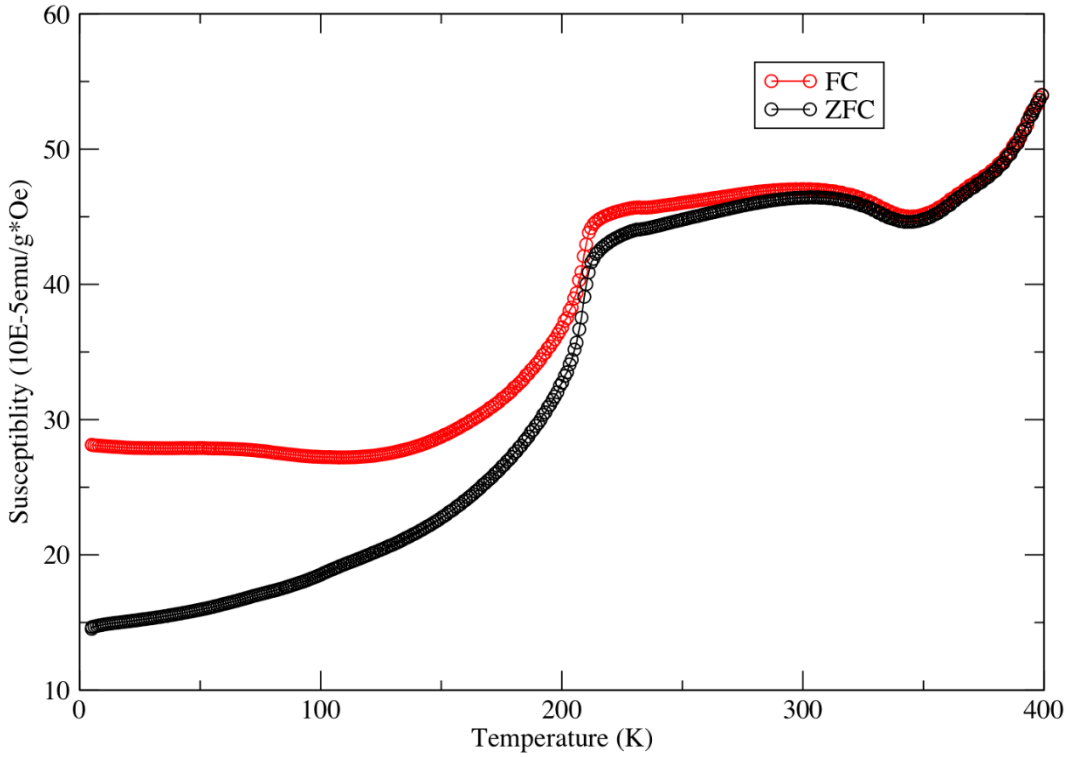

Fig. 22 Susceptibility versus temperature curves after zero field cooling (ZFC) and field cooling (FC) measured at 100 Oe applied fields.

3.2.6. DSC measurement

DSC measurements of Mn_3B_4 did not record obvious magnetic transition features as compared to Cu-Mn-As series compounds, which have big steps or sharp peaks. But small peaks near 400 K can still be seen in Fig. 23, which is consistent with MPMS-determined, known antiferromagnetic transition.

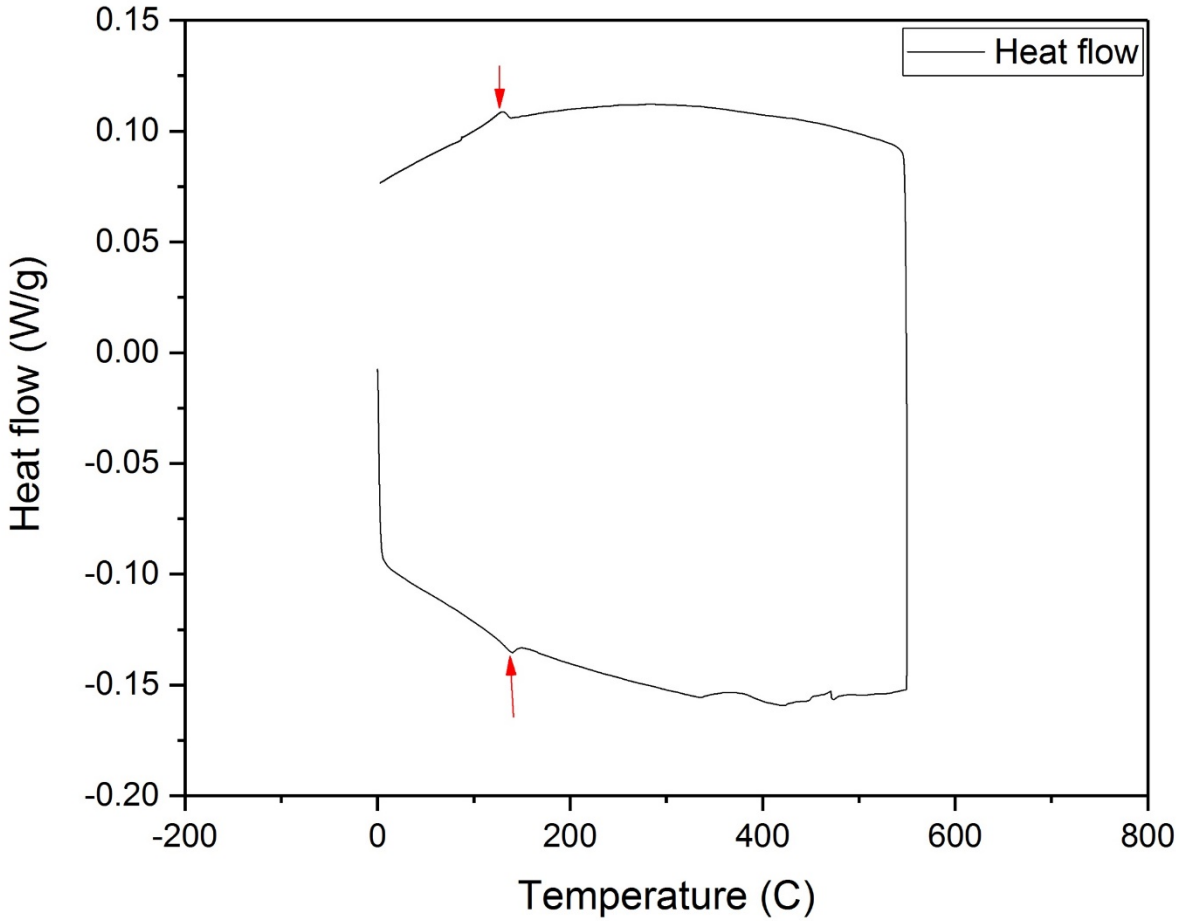

Fig. 23 DSC measurement of Mn_3B_4. The Néel temperature at 39K is arrowed.

CHAPTER 4
CONCLUSION

In this study, we seek to understand phase stability and transitions in the Cu-Mn-As ternary system, including a new hexagonal structure. The crystal structure of the new phase has been determined from single crystal diffraction, but the system warrants further testing to reconcile the single crystal and powder XRD data. DSC and MPMS measurements suggest a magnetic transition of this hexagonal phase near 330 K. The investigation of Cu-Mn-As phases shows that tetragonal phases dominates the Cu_2As-rich and Mn_2As-rich areas of the phase diagram. Specific trends among different compositions were observed. Both magnetic transition features (orthorhombic phase magnetic transition near 400 K and tetragonal phase magnetic transition at 520 K) show up in the DSC measurements, and the signals near 400 K fade away as the compositions deviate away from 1:1:1. The product with 1:1:1 composition is the orthorhombic phase. A plot of all the visible features observed in DSC measurements was provided for future reference, which indicates all the observed transitions in the 200 K to 800 K temperature range.

To obtain Mn_3B_4 single crystals with larger size, it is more effective to hold reactions at higher temperatures than increasing reaction times. Quartz tubes with smaller diameters and shorter sealed length are needed for reactions over 1200°C (or tubes of other materials could be used, such as alumina, platinum, etc.). Plates produced from this method are the orthorhombic Mn_3B_4 phase, but there are also needle shaped crystals which were found to be MnB. The impurity is invisible from powder X-ray diffraction, but can be differentiated based on their crystal shapes and single-crystal data.

References

[1]. L. Néel, in Nobel Lectures, *Physics* 1963–1970 318–341 (Elsevier, Amsterdam, 1972).

[2]. T. Jungwirth, X. Marti, P. Wadley and J. Wunderlich, Antiferromagnetic spintronics, *Nature Nano.* **11**, 231 (2016)

[3]. K. Olejnik et al. Antiferromagnetic CuMnAs multi-level memory cell with microelectronic compatibility. *Nat. Commun*. **8**, 15434 (2017).

[4]. Y. Bodnar et al. Writing and reading antiferromagnetic Mn_2Au by Néel spin-orbit torques and large anisotropic magnetoresistance. *Nat. Commun.* **9**, 348 (2018)

[5]. M. Meinert, D. Graulich, and T. Matalla-Wagner, Electrical switching of antiferromagnetic Mn_2Au and the role of thermal activation. Preprint version at arXiv:1706.06983 [cond-mat.mtrl-sci].

[6]. J. Sinova, S. O. Valenzuela, J. Wunderlich, C. H. Back, and T. Jungwirth, Spin Hall effects. *Rev. Mod. Phys*. **87**, 1213 (2015).

[7]. X. Zhang, Q. Liu, J. Luo, A. J. Freeman and A. Zunger, Hidden spin polarization in inversion-symmetric bulk crystals. *Nature Phys*. **10**, 387 (2014).

[8]. J. Železný et al. Relativistic Néel-Order Fields Induced by Electrical Current in Antiferromagnets. *Phys. Rev. Lett*. **113**, 157201 (2014).

[9]. P. Wadley, et al. Electrical switching of an antiferromagnet. *Science.* **351**, 587 (2016)

[10]. E. Emmanouilidou, H. Cao, P. Tang, X. Gui, C. Hu, B. Shen, J.Wu, S.Zhang, W. Xie, and N. Ni, Magnetic order induces symmetry breaking in the single-crystalline orthorhombic CuMnAs semimetal. *Phys. Rev. B.* **96**, 224405 (2017).

[11]. P. Wadley et al. Tetragonal phase of epitaxial room-temperature antiferromagnet CuMnAs. *Nature Comm.* **4**, 2322 (2013).

[12]. K. Uhlirová, R. Tarasenko, F. Javier Martínez-Casado, B. Vondracková, and Z. Matej, Synthesis and single crystal study of $CuMn_3As_2$ and $Cu_2Mn_4As_3$. *J. Alloys Compd.* **650**, 224 (2015).

[13]. P. C. Canfield and Z. Fisk, Growth of single crystals from metallic fluxes. *Philos. Mag. B* **65**, 1117 (1992).

[14]. F. Maca, J. Masek, O. Stelmakhovych, X. Marti, H. Reichlova, K. Uhlirova, P. Beran, P. Wadley, V. Novak, T. Jungwirth, Room-temperature antiferromagnetism in CuMnAs. *J. Magn. Magn. Mater.* **324**, 1606 (2012).

[15]. V. Hills, P. Wadley, R. P. Campion, V. Novak, R. Beardsley, K. W. Edmonds, B. L. Gallagher, B. Ouladdiaf, and T. Jungwirth, Paramagnetic to antiferromagnetic transition in epitaxial tetragonal CuMnAs. *J. Appl. Phys.* **117**, 172608 (2015).

[16]. Wadley, P. et al. Antiferromagnetic structure in tetragonal CuMnAs thin films. *Sci. Rep.* **5**, 17079 (2015).

[17]. M. Yuzuri and M. Yamada, On the magnetic properties of compound Mn_2As. *J. Phys. Soc. Japan.* **15**, 1845 (1960).

[18]. Y. Hwang, J. Choi, D. D. Dung, Y. Shin, and S. Cho, Perpendicular ferrimagnetism in strained Mn_2As film. *J. Appl. Phys*. **109**, 063914 (2011).

[19]. G. Dresselhaus, Spin-Orbit Coupling Effects in Zinc Blende Structures. *Phys. Rev.* **100**, 2, 580 (1955).

[21]. M. J. Benitez, O. Petracic, H. Tüysüz, F. Schüth, and H. Zabel, Fingerprinting the magnetic behavior of antiferromagnetic nanostructures using remanent magnetization curves. *Phys. Rev. B* **83**, 134424 (2011)

[22]. P. A. Joy et al, The relationship between field-cooled and zero-field-cooled susceptibilities of some ordered magnetic systems. *J. Phys.: Condens. Matter.* **10**, 11049 (1998).

[23]. J. Muendelein and H. U. Schuster. Darstellung und kristallstruktur der verbindungen MnCuX (X=P, As, P_xAs_{1-x}). *Z. Naturforsch. B* **47**, 925 (1992)

[24]. P. Wadley et al. Obtaining the structure factors for an epitaxial film using Cu X-ray radiation. *J. Appl. Crystallogr.* **46**, (6), 1749 (2013)

[25]. H. Hirota and A. Yanase. Magnetic Properties of Mn_3B_4. *J. Phys. Soc. Japan.* **20**, 1596 (1965)

[26]. S. Neov and E. Legrand. Neutron diffraction study of the magnetic structure of Mn_3B_4. *Phys. Stat. Sol*. **49**, 589 (1972)

[27]. Pierre Villars (Chief Editor), PAULING FILE in: Inorganic Solid Phases, Springer Materials (online database), Springer, Heidelberg (ed.) Springer Materials.